



RESEARCH ARTICLE

10.1002/2013MS000303

Key Points:

- Vertical resolution has a significant impact on the mean simulated climate
- Increased vertical resolution causes warming near the tropopause
- Vertical resolution and gravity waves impact surface stresses

Correspondence to:

J. H. Richter,
jrichter@ucar.edu

Citation:

J. H. Richter, A. Solomon, and J. T. Bacmeister (2014), Effects of vertical resolution and nonorographic gravity wave drag on the simulated climate in the Community Atmosphere Model, version 5. *J. Adv. Model. Earth Syst.*, 6, 357–383, doi:10.1002/2013MS000303.

Received 2 JAN 2014

Accepted 19 MAR 2014

Accepted article online 25 MAR 2014

Published online 27 MAY 2014

Effects of vertical resolution and nonorographic gravity wave drag on the simulated climate in the Community Atmosphere Model, version 5

Jadwiga H. Richter¹, Abraham Solomon², and Julio T. Bacmeister¹

¹Climate and Global Dynamics Division, National Center for Atmospheric Research, Boulder, Colorado, USA, ²Center for Ocean-Land-Atmosphere Studies (COLA)/Institute of Global Environment and Society (IGES), Fairfax, Virginia, USA

Abstract Horizontal resolution of general circulation models (GCMs) has significantly increased during the last decade, however these changes were not accompanied by similar changes in vertical resolution. In our study, the Community Atmosphere Model, version 5 (CAM5) is used to study the sensitivity of climate to vertical resolution and nonorographic gravity wave drag. Nonorographic gravity wave drag is typically omitted from low-top GCMs, however as we show, its influence on climate can be seen all the way to the surface. We show that an increase in vertical resolution from 1200 to 500 m in the free troposphere and lower stratosphere in CAM5 improves the representation of near-tropopause temperatures, lower stratospheric temperatures, and surface wind stresses. In combination with nonorographic gravity waves, CAM5 with increased vertical resolution produces a realistic Quasi-Biennial Oscillation (QBO), has an improved seasonal cycle of temperature in the extratropics, and represents better the coupling between the stratosphere and the troposphere.

1. Introduction

Horizontal and vertical resolution of general circulation models (GCMs) has increased significantly since the inception of climate models in the early 1980s. The first version of NCAR's Community Climate Model (CCM), CCM0, had only nine vertical levels with model top near 33 km and horizontal resolution of R15, or $\sim 4.4 \times 7.5^\circ$ [Pitcher et al., 1983]. CCM1 had R15 resolution but the number of levels increased to 12 to better represent the tropopause region [Randel and Williamson, 1990]. In CCM2, the number of vertical levels increased to 18 (with lid at 3 hPa) increasing the vertical resolution throughout the model domain (see Figure 1a) with default horizontal resolution increased to T42 or $2.8^\circ \times 2.8^\circ$ [e.g., Williamson and Rasch, 1994]. The default resolution of Community Atmosphere Model, version 3 (CAM3) remained at T42 [Collins et al., 2006] and the number of vertical levels increased to 26 with similar model lid (Figure 1a). Hence, CAM3 had horizontal resolution of ~ 300 km and vertical resolution of ~ 1.2 km in midtroposphere and lower stratosphere. The standard resolution for Community Atmosphere Model, version 4 (CAM4) has further increased significantly to $0.9^\circ \times 1.25^\circ$ (or ~ 100 km), whereas the vertical resolution remained at 26 levels [Neale et al., 2013]. Four levels were added in the boundary layer relative to the 26 level vertical structure of CAM3/CAM4 in CAM5 [Neale et al., 2012].

"Low-top" GCMs, or GCMs with model lids below 1 hPa [Charlton-Perez et al., 2013], developed by other modeling centers have similar configurations to that of CAM. For example, the GFDL CM3 model [Donner et al., 2011] has resolution of $2^\circ \times 2.5^\circ$ with vertical resolution of ~ 1 km in midtroposphere. The Hadley Centre Global Environmental Model version 2 (HadGEM2) $1.25^\circ \times 1.875^\circ$ with 38 layers in the vertical extending to over 39 km in height [Collins et al., 2011]. Although increased horizontal resolution of GCMs has been the primary focus of newer generation GCMs, it is important to understand that vertical resolution consistent with horizontal resolution is needed to properly represent the atmospheric motions that are being resolved in the horizontal with finer horizontal resolutions. Lindzen and Fox-Rabinovitz [1989] developed simple criteria for consistency between vertical and horizontal resolution in general circulation models. For extratropical quasi-geostrophic disturbances, Lindzen and Fox-Rabinovitz [1989] argue that the vertical model grid spacing, Δz should be related to the horizontal model grid spacing, Δx by the following relation:

$$\frac{\Delta z}{\Delta x} = \frac{f}{N} \quad (1)$$

This is an open access article under the terms of the Creative Commons Attribution-NonCommercial-NoDerivs License, which permits use and distribution in any medium, provided the original work is properly cited, the use is non-commercial and no modifications or adaptations are made.

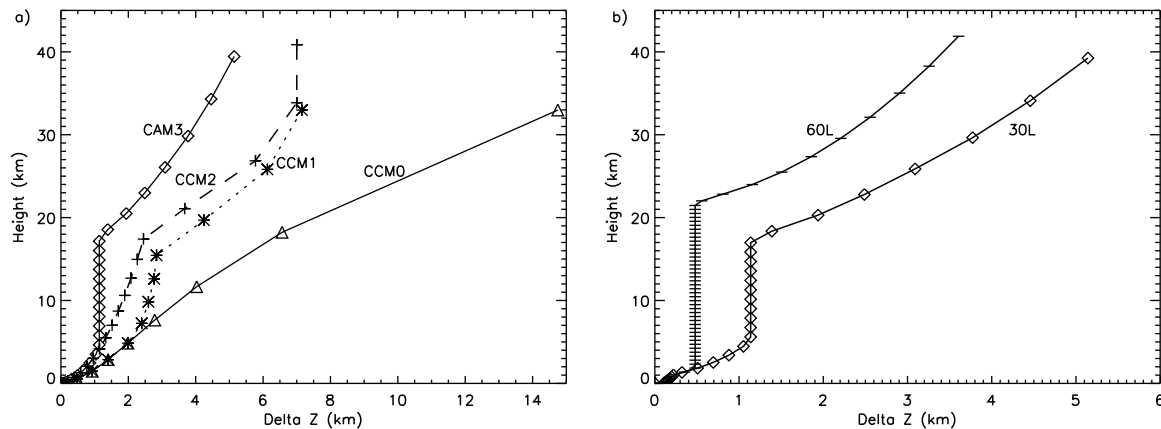


Figure 1. Approximate vertical grid spacing in km used in Figure 1a previous versions of NCAR's GCM: CCM0 (triangles), CCM1 (asterisks), CCM2 (plus signs), CAM3 (diamonds), and (b) CAM5 simulations with 30 levels (diamonds) and 60 levels (minus signs).

where f is the Coriolis parameter and N is the Brunt-Väisälä frequency. At 45°N , f is approximately $1\text{e}^{-4}\text{ s}^{-1}$, N is 0.012 s^{-1} in the troposphere, and 0.022 s^{-1} in the stratosphere. In the troposphere then, $f/N \sim 0.005$, and in the stratosphere, $f/N \sim 0.0086$. Therefore, vertical grid spacing should be ~ 116 times smaller and ~ 200 times smaller than horizontal grid spacing to adequately resolve motions in the troposphere and stratosphere adequately. Hence, for GCM horizontal resolutions of $\sim 200\text{ km}$, vertical resolution of $\sim 1\text{ km}$ is appropriate, whereas for horizontal resolution of $\sim 100\text{ km}$, vertical resolution of 500 m is appropriate if stratospheric and tropospheric motions are to be resolved. Unfortunately, in the development of climate models, these simple recommendations of Lindzen and Fox-Rabinovitz [1989] are seldom the guiding principles behind the vertical structure development in climate models.

Several studies have examined the effects of increased vertical resolution on the simulation of climate in a GCM. Pope *et al.* [2001] found upper tropospheric and stratospheric temperature increase, tropical temperatures decrease, and equatorward movement of westerly jets as a result of increasing vertical resolution from ~ 2 to $\sim 1\text{ km}$ in a $2.5^{\circ} \times 3.75^{\circ}$ version of the Hadley Center Climate Model. Roeckner *et al.* [2006] found that increasing vertical resolution leads to a cooling of the tropopause region, tropospheric cooling in low to middle latitudes, and warming in high latitudes and close to the surface. They also found that increasing vertical resolution results in a pronounced warming in the polar upper troposphere and lower stratosphere. Rind *et al.* [2007] found that increased vertical resolution had significant impact on tracer transport mainly due to faster interhemispheric transport associated with stronger Hadley circulation and increased tropical eddy kinetic energy.

The vertical resolution of a model has been shown to be crucial to representing convectively coupled equatorial waves (CCEWs) and the tropical lower stratospheric Quasi-Biennial Oscillation (QBO) [e.g., Boville and Randel, 1992; Giorgi *et al.*, 2002]. In particular, Mixed-Rossby gravity waves and equatorial Kelvin waves are crucial to the driving of the QBO. These waves have vertical wavelengths that range from ~ 3 to 8 km and hence the small vertical wavelength range of the wave spectra is not well represented in GCMs with vertical resolution of only $\sim 1\text{ km}$. A detailed examination of simulated CCEWs and the ability of CAM5 with higher vertical resolution and gravity waves to represent a QBO is presented in a separate publication [Richter *et al.*, 2014].

Nonorographic gravity wave parameterizations have become a standard part of "high-top" (model top above 1 hPa) GCMs such as HAMMONIA [e.g., Schmidt *et al.*, 2006] and the Whole Atmosphere Community Climate Model (WACCM) [e.g., Richter *et al.*, 2010]. This is due to the large amount of momentum that these waves deposit in the stratosphere and mesosphere and their contribution to the driving of residual circulations. "Low-top" GCMs, with their primary focus on modeling the troposphere and lower stratosphere have typically omitted GW parameterization with the exception of orographic GWs. A study of Coupled Model Intercomparison Project Phase 5 (CMIP5) models by Charlton-Perez *et al.* [2013] revealed that only one of the 11 "low-top" GCMs had a nonorographic gravity wave parameterization. In all previous versions, CAM

has also only included a parameterization of orographic gravity wave drag. Although the primary domain of interest of typical CAM users is the troposphere, the model domain does include the stratosphere, and better representation of the stratosphere could improve the representation of tropospheric climate. Hence, in addition to vertical resolution, we examine here the effects of nonorographic gravity wave drag on the mean climate and variability of the troposphere and lower stratosphere. In our simulations, we examine both the mean tropospheric and lower stratospheric climate, as well as variability of the tropics and the extratropics.

2. Model Description

In our study, we use the Community Atmosphere Model, version 5 (CAM5). A complete description of CAM5 is given by *Neale et al.* [2012] and we describe below the key features of CAM5. The version of CAM5 used in this study utilized the new spectral element (SE) dynamical core [*Dennis et al.*, 2012]. SE is a highly scalable core which uses a cubed-sphere geometry and continuous Galerkin spectral element techniques [*Taylor and Fournier*, 2010]. This dynamical core is expected to become the default for CAM5 in the near future.

CAM5 uses the moist planetary boundary layer (PBL) turbulent transport parameterization according to *Bretherton and Park* [2009]. A plume-based treatment of shallow-convection is used [*Park and Bretherton*, 2009]. Deep convection is parameterized using the *Zhang and McFarlane* [1995] parameterization. CAM5 incorporates an advanced two-moment representation of cloud microphysical processes [*Morrison and Gettelman*, 2008; *Gettelman et al.*, 2010] that is directly coupled to prognostic aerosol mass and number concentrations predicted by a comprehensive modal aerosol model [*Easter et al.*, 2004; *Ghan and Easter*, 2006]. Radiative heating and cooling are treated using the GCM version of the “Rapid and Accurate Radiative Transfer Model” (RRTM) [*Iacono et al.*, 2008].

2.1. Control Simulation

The default vertical structure of CAM5 consists of 30 vertical levels with approximately 1200 m vertical spacing throughout the free troposphere and lower stratosphere with model top at ~ 2 hPa (Figure 1b). The default horizontal resolution for CAM5 has 30 spectral elements on each side of a cubed-sphere face (ne30). A third-order polynomial representation is used in each element, which results in a horizontal resolution of ~ 100 km. This default model setup is our control simulation and will be hereafter referred to as 30Lcam. This standard configuration of CAM5 includes an orographic gravity wave parameterization following *McFarlane* [1987]. A parameterization of nonorographic gravity wave drag is not included.

2.2. Experiment Simulations

In order to explore the effects of vertical resolution on CAM5’s climate, we have set up a simulation with 60 vertical levels, 60Lcam. The vertical level structure for this simulation is shown by the dotted line in Figure 1b. In 60Lcam, we decrease the vertical grid spacing to ~ 500 m above 850 mb. This simulation only explores effects of vertical resolution in the free troposphere and the stratosphere. Effects of increasing vertical resolution in the planetary boundary layer will be explored in the future.

Effects of nonorographic gravity wave drag are explored here by adding the GW parameterization from WACCM [*Richter et al.*, 2010] into CAM. The nonorographic GW parameterization assumes that gravity waves are generated by two dominant sources: fronts and convection. Gravity waves are launched only when a gravity wave source is detected. Frontally generated gravity waves are launched when the frontogenesis function [*Hoskins*, 1982] exceeds a critical threshold. At every point and time step of the model when the criteria are met, a broad spectrum of gravity waves is launched and propagated through the atmosphere using the *Lindzen* [1981] parameterization. All settings of the frontal source spectrum parameterization follow *Richter et al.* [2010]. Similarly, every time the deep convection scheme of *Zhang and McFarlane* [1995] is active, a spectrum of convectively generated gravity waves is launched. The source spectrum of convectively generated waves is dependent on the heating depth, amplitude, and mean wind in the convective heating region following the parameterization of *Beres et al.* [2004]. One of the tunable parameters in the *Beres et al.* [2004] parameterization is the efficiency factor, which can be thought of as the fraction of the model grid box covered by gravity waves. This parameter was set to 0.1 in *Richter et al.* [2010]. We use a convective GW efficiency of 0.55 here. This increase in GW efficiency from *Richter et al.* [2010] can be justified by the increased horizontal resolution in our model (100 versus 200 km), and hence bigger probability

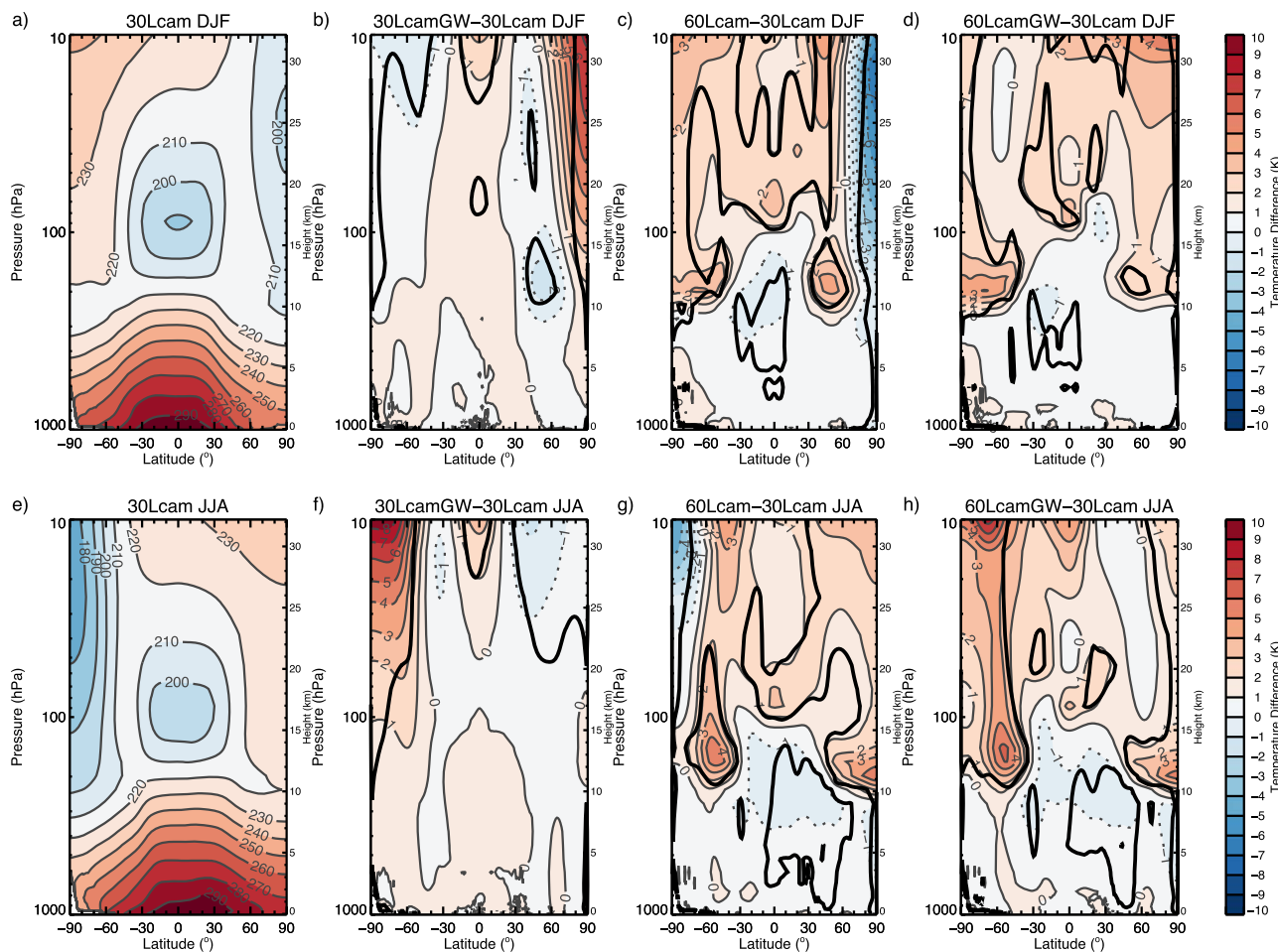


Figure 2. (a and e) Temperature in 30Lcam and (remaining plots) temperature difference from 30Lcam for various CAM5 simulations. (top) DJF average and (bottom) JJA average. Units are degrees Kelvin. Contours are clearly labeled in Figures 2a and 2e. Color bar shown applies to the three rightmost plots in each row. Black thick line depicts the regions that are significant at the 99% level according to the Student's *t* test.

that a large fraction of the model grid box is occupied by convection. This setting also gives the best simulation of the tropical Quasi-Biennial Oscillation [Richter et al., 2014]. As gravity waves generated by deep convection are mostly confined to the Tropics [Richter et al., 2010], the change in convective GW efficiency has almost no impact on the extratropical climate. Shaw and Shepherd [2007] showed that violation of angular momentum conservation in a general circulation model can lead to spurious circulations in the model domain. Following the recommendation of Shaw and Shepherd [2007], any remaining GW momentum of parameterized gravity waves at the top of the model domain is deposited in the top layer of the model. We carry out simulations with nonorographic gravity waves both with the 30 and the 60 layer model. The simulations are called 30LcamGW and 60LcamGW, respectively.

3. Mean Temperature and Zonal Wind Structure

In this section, we describe the changes to mean climate in CAM5 as a result of increased vertical resolution and added gravity wave drag parameterization. We exclude from our discussion the last three layers of the model (above 10 hPa) which have coarser vertical resolution and extra dissipation.

3.1. Control Simulation

Figures 2a and 2e show the 20 years (1980–1999) average December, January, February (DJF) and average June, July, August (JJA) temperature for 30Lcam, respectively. Tropospheric temperature decreases steadily

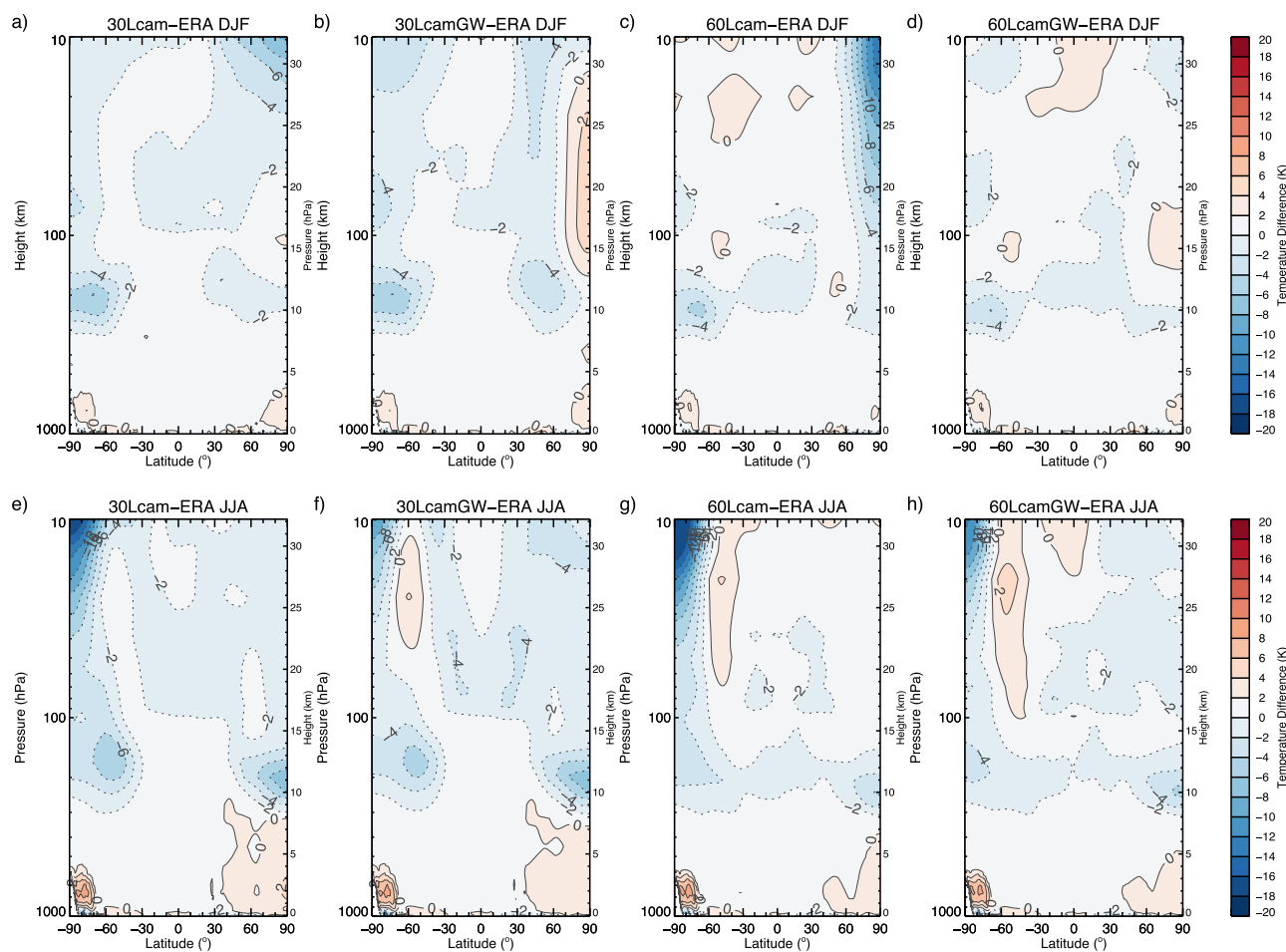


Figure 3. Temperature difference from ERA Interim (1980–1999) for 30Lcam, 30LcamGW, 60Lcam, and 60LcamGW. (top) DJF and (bottom) JJA. Contour interval is 2 K.

up to the tropopause reaching a cold point of 188.5 K in DJF and 194 K in JJA at the equator. In the global mean, the temperature of the stratosphere increases with altitude; however, there is a strong annual cycle of temperature. The winter polar temperature in the lower stratosphere is 20–40 K lower than in summer. Stratospheric temperatures are in large part driven by the mean meridional circulation which causes upward motion (cooling) in the tropics, and downward motion (compressional warming) in the winter hemisphere polar regions [Andrews *et al.*, 1987].

30Lcam captures the general features of the mean tropospheric and stratospheric temperature structure; however, it does carry some biases relative to observations. Figures 3a and e show the DJF and JJA temperature difference relative to the ERA-Interim data set [Dee *et al.*, 2011]. CAM5 temperatures near the tropopause and in the lower stratosphere are colder than in observations. The largest biases occur near the summer tropopause: 6 K in DJF (Figure 3a), and more than 8 K in JJA (Figure 3e). This cold high-latitude tropopause bias is also found in other GCMs [Solomon *et al.*, 2007, chap. 8.3.1.1]. The tropical tropopause in CAM5 is about 2 K too cold with respect to ERA Interim reanalyses, similarly to previous versions of the NCAR GCM [Collins *et al.*, 2006; Neale *et al.*, 2013]. The lower stratosphere in CAM5, between 10 and 100 hPa is also colder than observed. Here the largest biases are seen in the winter hemisphere, especially in JJA, reaching –18 K at the South Pole.

Zonal mean wind for the 30Lcam simulation is shown in Figures 4a and 4e and the biases relative to ERA are shown in Figures 5a and 5e. The tropospheric zonal mean wind is in good agreement with observations, however similarly to the temperature field, CAM5's biases grow above 200 hPa. In DJF, the tropospheric

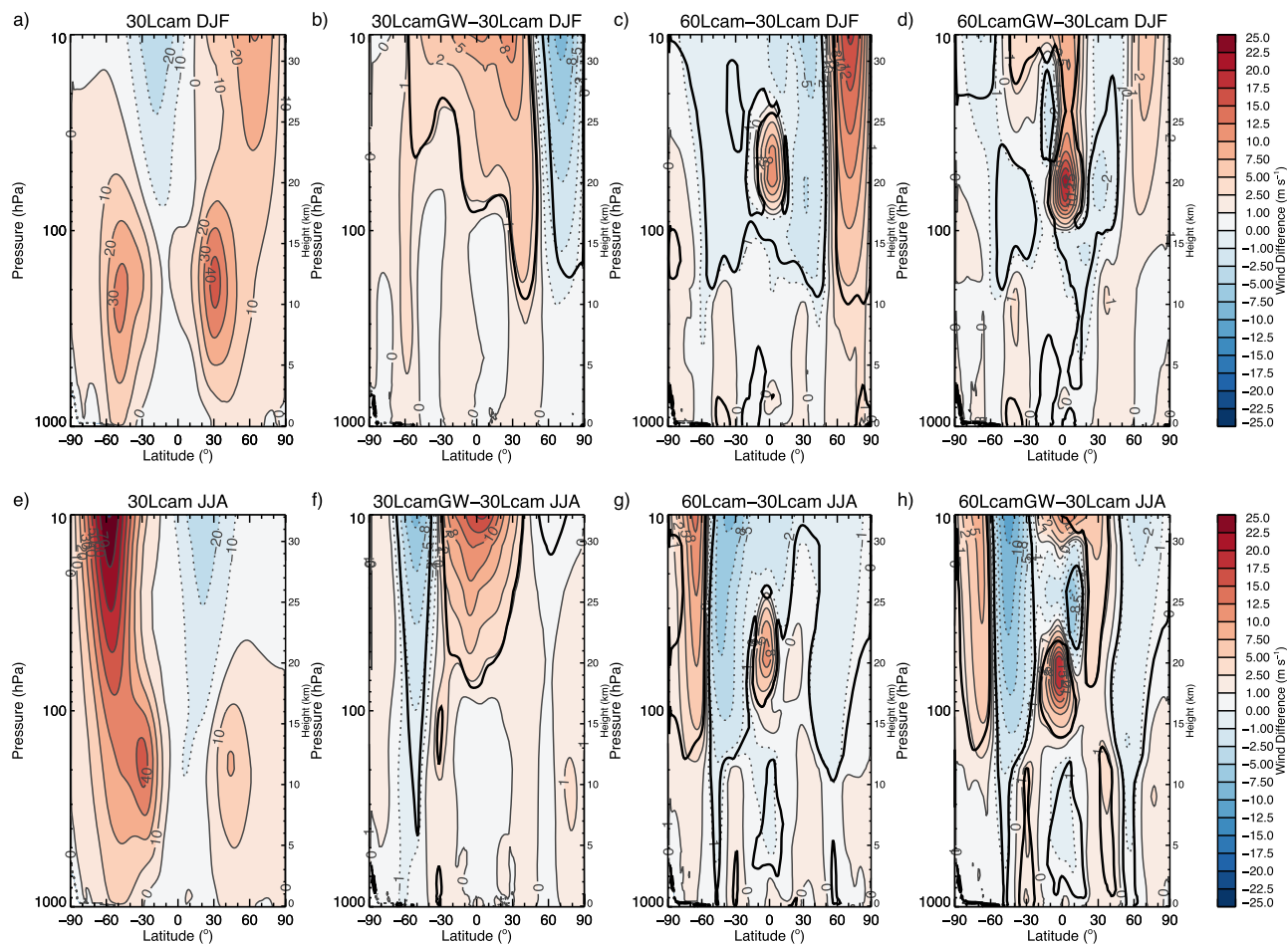


Figure 4. Same as in Figure 2 but for zonal mean wind. Units are m s^{-1} .

summer jet extends too far into the stratosphere, causing a mean wind bias of over 4 m s^{-1} throughout the upper troposphere and lower stratosphere near 60°S . In the Northern Hemisphere winter the stratospheric westerly jet is too close to the equator, causing upper tropospheric and lower stratospheric winds to be too strong near 30°N and too weak near 60°N . In JJA, in the Southern Hemisphere, the stratospheric jet is too strong by up to 8 m s^{-1} , and the Northern Hemisphere's winds in the extratropics are too strong by about 2 m s^{-1} from 200 to 10 hPa.

3.2. Effects of Gravity Waves

We begin our sensitivity studies by looking at the effects of nonorographic gravity waves on the mean tropospheric and lower stratospheric climate. Gravity wave amplitudes increase exponentially with height and hence their largest impacts are in the mesosphere and lower thermosphere [e.g., Fritts and Alexander, 2003], unless they encounter a critical level below. However, gravity waves can deposit a small amount of momentum in the stratosphere that can be important to the mean wind and temperature structure in this region. Also, when the momentum due to nonorographic gravity waves is deposited near the model top to conserve momentum [Shaw and Shepherd, 2007; Shaw et al., 2009], the circulation below is affected via downward control [Haynes et al., 1991].

Figures 2b and 2f show the change in the mean temperature in the 30LcamGW compared to 30Lcam. In DJF, the temperature in the polar Northern Hemisphere upper troposphere and lower stratosphere warms by up to 7 K. There is also cooling of ~ 1 K between 20 and 10 hPa between 60°S and 90°S . In JJA, we see similar changes: the region between 100 and 10 hPa, south of 60°S warms by up to 8 K, and there is cooling of 1–2 K between 20 and 10 hPa in the summer hemisphere. In both seasons, there is warming of 1–2 K in

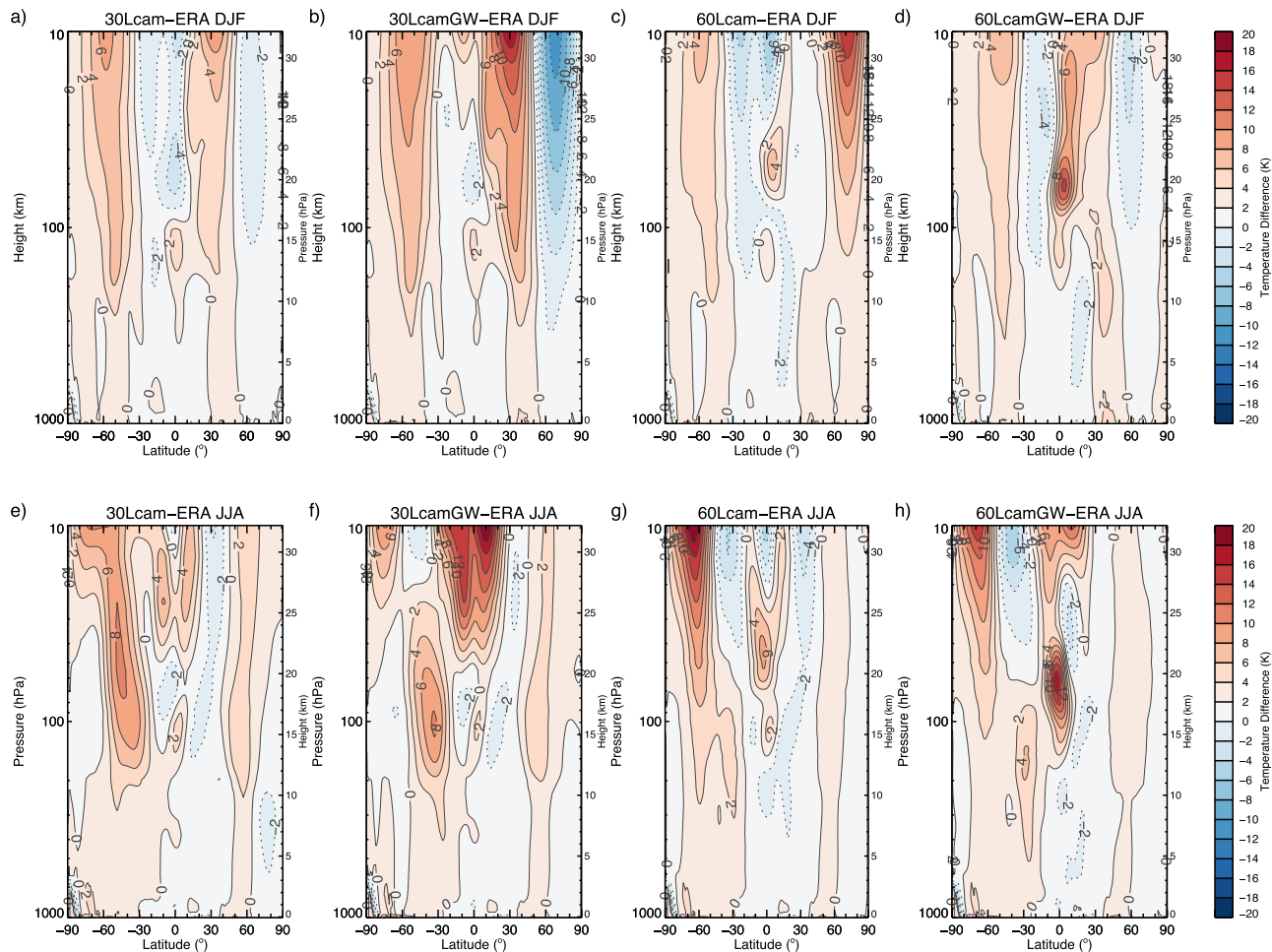


Figure 5. Same as Figure 3 but for zonal mean wind. Contour interval is 2 m s^{-1} .

the tropics, between 20 and 10 hPa. The winter polar warming in 30LcamGW helps to alleviate CAM5's cold bias in the polar stratosphere (Figures 3b and 3f); however, the warming in this region is so large that it actually introduces a warm bias between 150 and 30 hPa in DJF near the North Pole. In JJA (Figure 3f), the cold polar stratosphere bias is reduced by 50%, and near 60°S , 20 hPa the temperatures actually become slightly warmer than those observed. The large warming near the winter pole in 30LcamGW is associated with changes the stratospheric westerly jet: in both DJF and JJA, the stratospheric jet moves equatorward (Figures 4b and 4f).

The changes in 30LcamGW relative to 30Lcam can be explained using the Transformed Eulerian Mean (TEM) framework [Andrews *et al.*, 1987]. The residual mean meridional circulation is defined by the mean residual meridional velocity, \bar{v}^* , and the mean residual vertical velocity, \bar{w}^* :

$$\bar{v}^* \equiv \bar{v} - \rho_0^{-1} (\rho_0 \bar{v}' \theta' / \bar{\theta}_z)_z \quad (2)$$

$$\bar{w}^* \equiv \bar{w} + (a \cos \phi)^{-1} (\cos \phi \bar{v}' \theta' / \bar{\theta}_z)_\phi \quad (3)$$

where v and w are the simulated meridional and vertical velocities, ρ_0 is the atmospheric density, θ is the potential temperature, a is the radius of the earth, and ϕ is the latitude. In the above, an overbar represents a zonal mean and departures from the zonal mean are denoted by primes.

Changes in the mean residual circulation occur due to changes in resolved wave forcing, typically described in terms of the Eliassen-Palm flux (EP flux), denoted by \mathbf{F} , and unresolved gravity wave drag (or other drag

on the mean flow) denoted by \bar{X} . The meridional and vertical components of the EP flux vector, \mathbf{F} , are defined as follows:

$$F^{(\phi)} \equiv \rho_0 a \cos\phi (\bar{u}_z \overline{v' \theta'} / \bar{\theta}_z - \overline{v' u'}) \quad (4)$$

$$F^{(z)} \equiv \rho_0 a \cos\phi \left\{ \left[f - (a \cos\phi)^{-1} (\bar{u} \cos\phi)_\phi \right] \overline{v' \theta'} / \bar{\theta}_z - \overline{w' u'} \right\} \quad (5)$$

where f is the Coriolis parameter. EP flux divergence is defined as:

$$\nabla \cdot \mathbf{F} \equiv (a \cos\phi)^{-1} \frac{\partial}{\partial \phi} (F^{(\phi)} \cos\phi) + \frac{\partial F^{(z)}}{\partial z} \quad (6)$$

and the zonal momentum equation showing the relationship between EP flux divergence, parameterized wave drag, and mean circulation reads as follows:

$$\bar{u}_t + \bar{v}^* \left[(a \cos\phi)^{-1} (\bar{u} \cos\phi)_\phi - f \right] + \bar{w}^* \bar{u}_z = (\rho_0 a \cos\phi)^{-1} \nabla \cdot \mathbf{F} + \bar{X} \quad (7)$$

According to the above, changes in gravity wave drag (\bar{X}), will result in changes in the mean residual circulation. Figure 6 shows the orographic and nonorographic gravity wave drag in the 30LcamGW simulation. This figure shows that below 10 hPa, gravity wave drag comes only from orographic gravity waves, and is only active in the winter hemisphere where near stationary waves can propagate upward. Nonorographic gravity waves have low amplitudes in the stratosphere and hence their momentum is only deposited in the top layer of the model domain (with the enforcement of the momentum flux going to zero at model top). The force on the mean flow from nonorographic gravity waves reaches amplitudes of $3 \text{ m s}^{-1} \text{ d}^{-1}$ in DJF and $5 \text{ m s}^{-1} \text{ d}^{-1}$ in JJA. Eastward (positive) GW drag appears in summer hemisphere and westward (negative) GW drag appears in the winter hemisphere. In the winter hemisphere, many of the gravity waves with positive phase speeds reach their critical levels in the westerly jet, and hence there is a dominance of westward propagating gravity waves at the model top. In the summer hemisphere, the situation is reversed. The nonorographic gravity wave drag near the model top is split fairly equally between convective and frontally generated waves (not shown): convective gravity wave drag dominates in the tropics, and frontal gravity wave drag dominates in the extratropics [Richter et al., 2010].

The addition of nonorographic gravity wave drag in 30LcamGW induces changes in the residual mean meridional circulation. These changes are illustrated in Figures 7 and 8 for DJF and JJA, respectively. The mean residual circulation is directed upward in the Tropics, toward the winter pole in midlatitudes, and downward over the winter pole. The addition of nonorographic gravity wave drag strengthens this circulation by increasing the meridional residual velocity near the model top (Figures 7b and 8b) and increasing the downward motion over the winter pole (Figures 7f and 8f). The increased downward motion extends down to 100 hPa in DJF and to 60 hPa in JJA and causes compressional warming, explaining the increase in temperatures near the winter pole in the upper troposphere and lower stratosphere. Hence, although gravity waves do not deposit momentum directly in this region, they can significantly impact the mean temperature structure via downward control [Haynes et al., 1991]. Shaw et al. [2009] showed that including momentum conservation in a GCM with a top near 10 hPa is very important as its effects reach all the way down to the surface. Shaw et al. [2009] also showed that including momentum conservation for non orographic waves brings the simulated climate in closer agreement with a high-top version of the same model.

Although the dominant response to nonorographic gravity wave drag in CAM5 is dynamical, it is worthwhile to note that there is a small change to the radiative forcing in 30LcamGW as compared to 30Lcam. This is easily understood by considering changes in water vapor between the two simulations shown in Figures 9b and 9f. In 30LcamGW, there is an increase in water vapor concentration in JJA, between 75°S and 90°S and between 100 and 10 hPa. As this change in water vapor occurs in the same location as the large warming seen in Figure 2f, we conclude that the change in stratospheric temperatures in JJA in 30LcamGW partially comes from the change in the radiative effects water vapor. In DJF, the water vapor distribution between 30Lcam and 30LcamGW is unchanged.

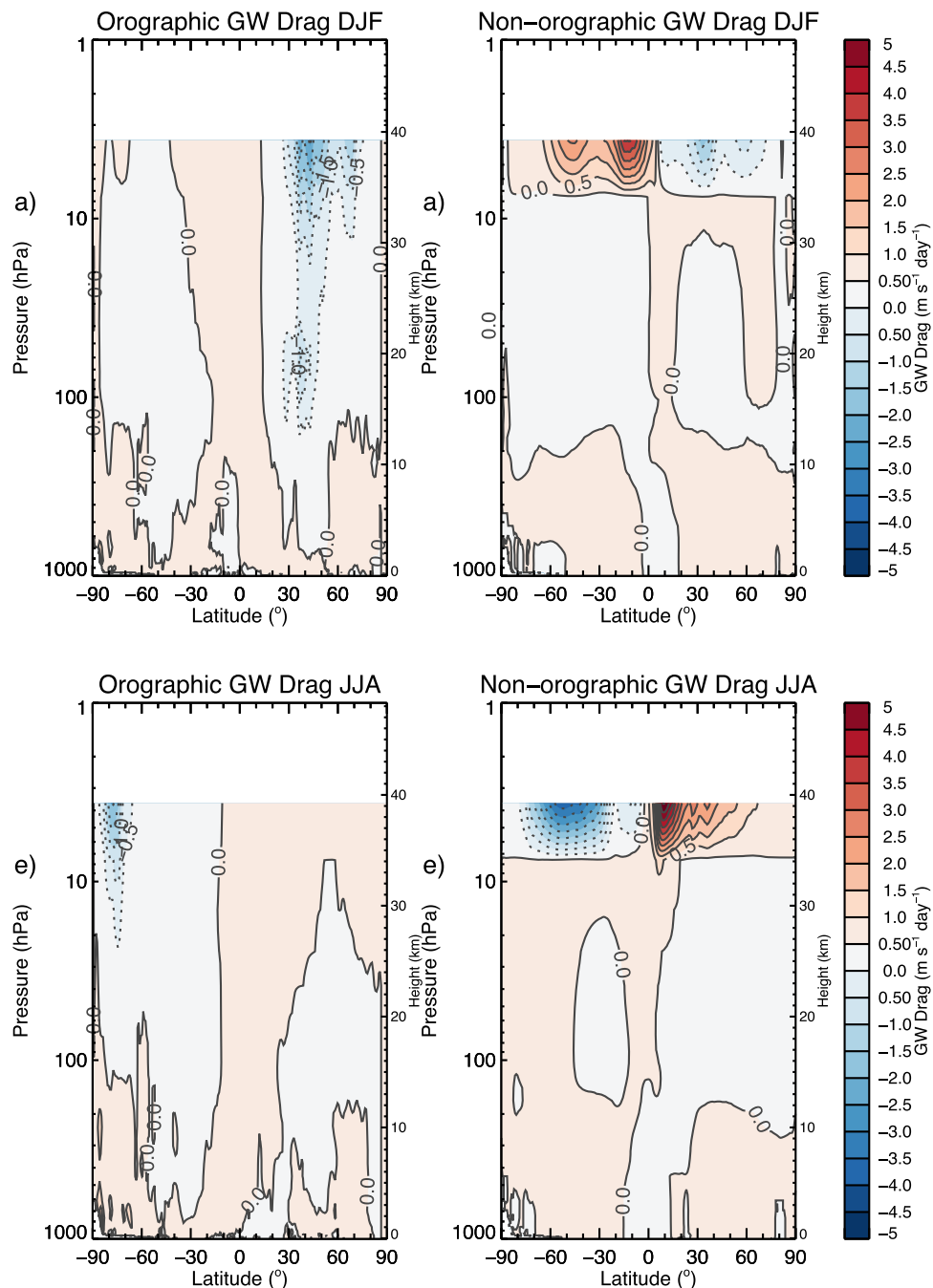


Figure 6. (left) Gravity wave drag due to orographic and (right) nonorographic gravity waves in the 30LcamGW simulation. (top) DJF average and (bottom) JJA average. Contour interval is $0.5 \text{ m s}^{-1} \text{ day}^{-1}$.

3.3. Effects of Vertical Resolution

Figures 2c and 2g show the change in the mean temperature in the 60Lcam compared to 30Lcam. Recall that there are no physics or tuning changes between these two models; the only difference is the vertical grid spacing. In DJF (Figure 2c), increased vertical resolution causes large cooling in winter polar region in the upper troposphere and lower stratosphere. This cooling has a magnitude of 3–4 K near 100 hPa and exceeds 7 K near 20 hPa. There is also cooling of ~1 K in the tropics between 250 and 150 hPa. The lower stratosphere and the extratropical tropopause region experiences warming of 1–3 K. Most of this warming

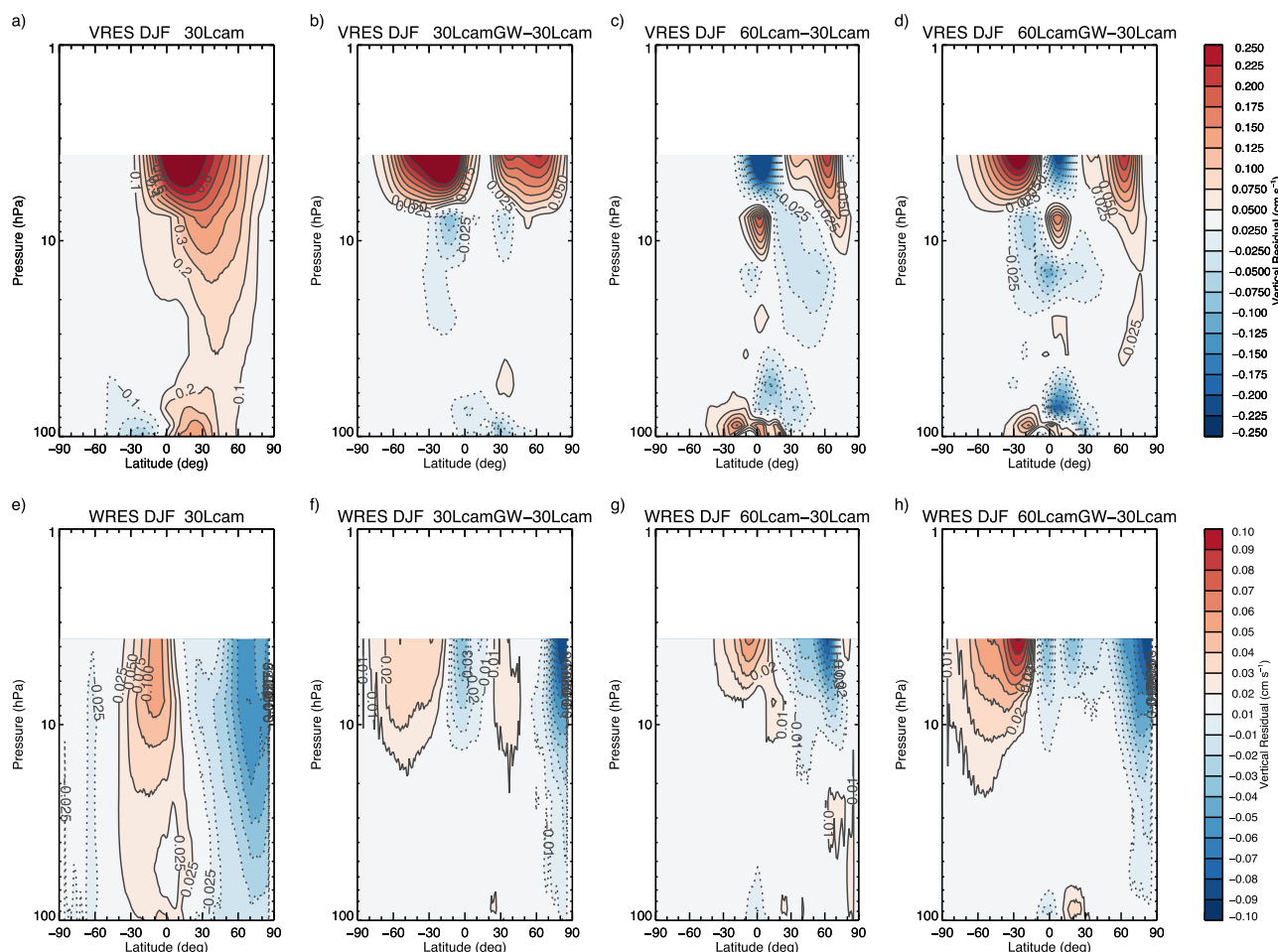


Figure 7. (top) Meridional and (bottom) vertical DJF residual velocity in (left) 30Lcam and (remaining plots) the difference from 30Lcam. The contour interval is (top left) 0.1 m s^{-1} for meridional velocity and (bottom left) 0.025 cm s^{-1} for vertical velocity. Contour interval for meridional (vertical) residual velocity difference plots is 0.025 m s^{-1} (0.01 cm s^{-1}). Color bars are for the difference plots only.

is significant at the 99% confidence level using the Student's *t* test. In JJA (Figure 2g), the temperature changes relative to the control simulation are similar, although, the polar stratospheric cooling is smaller and the extratropical tropopause warming is nearly doubled with temperatures at 150 hPa, 60°S and at 200 hPa, 85°N over 4 K warmer than in 30Lcam.

The increase in the model's vertical resolution decreases CAM5's temperature biases near the tropopause. This occurs both in DJF and JJA (Figures 3c and 3g). In the Southern Hemisphere, summer and winter and in the Northern Hemisphere summer, the tropopause bias near 200 hPa is reduced by 2 K. Throughout the lower stratosphere, the overall cold bias is also reduced, except in the polar-most winter stratosphere, where the cold temperature bias relative to ERAI increases significantly.

Zonal mean wind is related to the temperature through the thermal wind relationship; hence, we expect large changes in the zonal mean wind in the vicinity of changes in the mean temperature structure of the atmosphere. In 60Lcam, the temperature gradient near 60°N is intensified in DJF (Figure 2c) and we see large changes in the stratospheric westerly jet in this region (Figure 4c). In 60Lcam, the upper tropospheric and lower stratospheric winds between 60°N and 90°N increase between 5 and 20 m s^{-1} (between 200 and 10 hPa). The jet maximum also shifts toward the pole, and there is a decrease in the upper tropospheric/lower stratospheric winds between 10°N and 40°N . In the summer hemisphere winter, similar changes are seen (Figure 4g) but they are weaker, as the change in the extratropical temperature gradient between 60Lcam and 30Lcam was weaker in JJA.

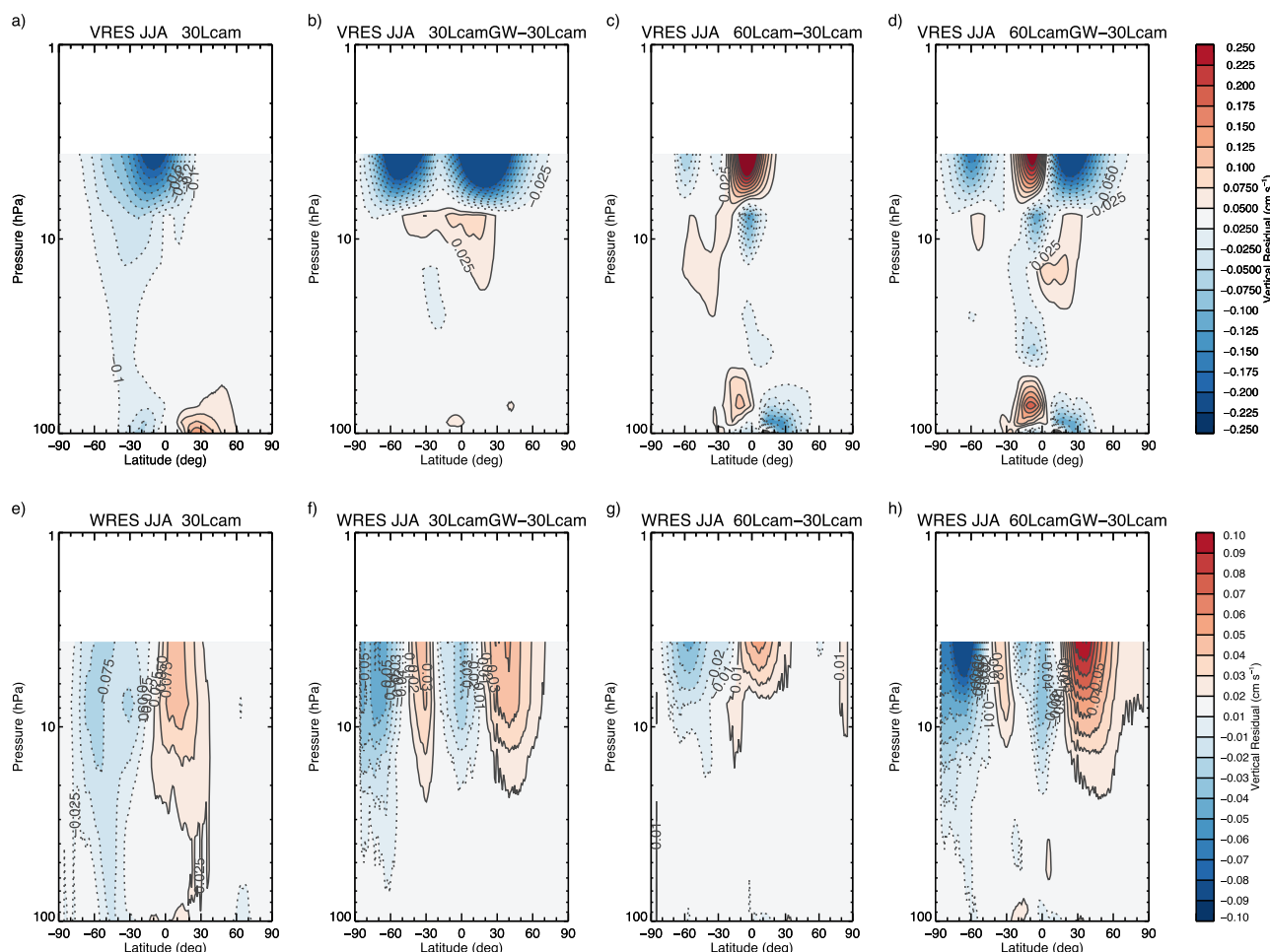


Figure 8. Same as Figure 7 but for JJA.

The reasons for temperature differences between the 60 level and 30 level CAM5 are not as straightforward to explain as the differences resulting from adding gravity wave drag into the 30L model. In 60Lcam, there is no nonorographic GW drag, so the primary changes to the residual mean circulation should occur as a result of resolved wave forcing, or EP flux divergence. In addition, the changes in 60Lcam take place through the majority of the upper troposphere and lower stratosphere, hence they all cannot be attributed to changes in the residual circulation; some come from changes in the radiative forcing in the model. First, we examine the changes in EP flux divergence for 60Lcam and 30Lcam (Figure 10) and then we consider the entire temperature budget for various regions of the atmosphere.

Figure 10 shows that EP flux divergence contributes to the stratospheric momentum budget in the winter hemisphere. We expect this as extratropical quasi-stationary planetary waves can only propagate in westerly winds. In the stratosphere, the differences between EP flux divergence between the 60Lcam and 30Lcam are small, $0.5 \text{ m s}^{-1} \text{ d}^{-1}$ around 10 hPa, and up to $-1.5 \text{ m s}^{-1} \text{ d}^{-1}$ at the very model top. As the changes in EP flux divergence are small, especially considered to the momentum changes due to the gravity wave drag in 30LcamGW, the resulting changes in stratospheric residual circulation are also small. Figures 7c, 7g, 8c, and 8g confirm this and show that residual vertical and meridional velocity changes, especially below 10 hPa in 60Lcam are very small. Above 10 hPa, there is an intensification of the residual vertical velocity both in DJF and JJA. More specifically, the downward branch of the residual circulation is intensified near 60°N in DJF and near 60°S in JJA, suggesting that to be the contributing factor to stratospheric warming in this region. However, these changes do not explain all of the temperature differences between 60Lcam and 30Lcam. It is important to note, that there are also significant changes in the EP flux

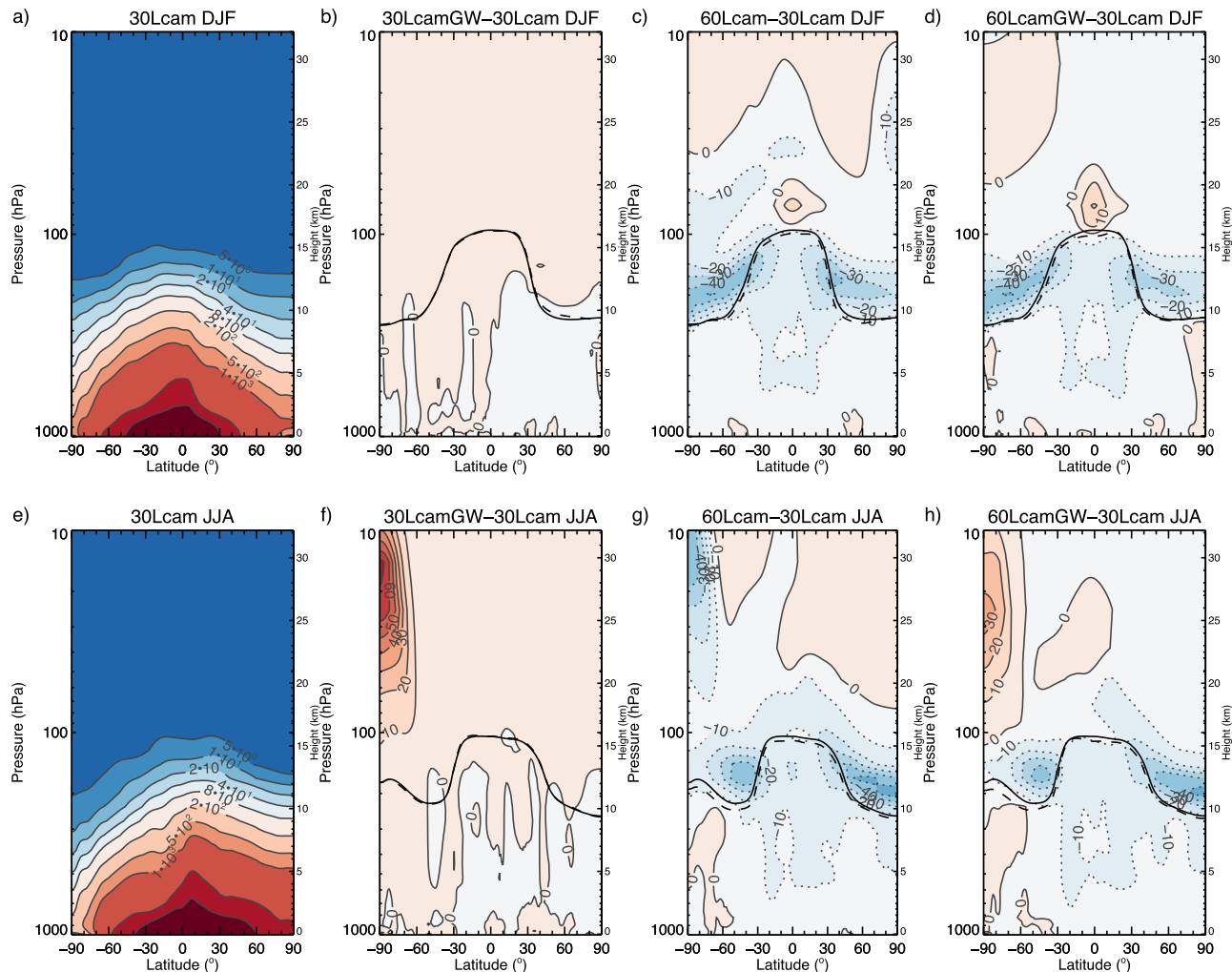


Figure 9. Water vapor mixing ratio in ppmv for (left plots) 30Lcam and (remaining plots) water vapor mixing ratio difference from 30Lcam for various CAM5 simulations in %. (top) DJF average and (bottom) JJA average. Contours in the left plots are: 5, 10, 20, 40, 80, 2×10^2 , 5×10^2 , 1×10^3 , 5×10^3 , 1×10^4 , and 5×10^4 . Contours are in equal intervals of 10% in the remaining plots. Tropopause height is depicted in the solid line for 30Lcam and dashed line for the various CAM5 simulations.

divergence in the upper troposphere between 60Lcam and 30Lcam. The amplitude of these changes is between 30% and 50% of the EP flux in 30Lcam in this region. The EP flux divergence changes are both positive and negative implying that both wave generation and dissipation is affected. Wave generation and propagation are dependent on many factors, such as the distribution of large-scale heating, instabilities, and the wind through which the waves propagate through. Hence, the cause and effect of the EP flux differences between 60Lcam and 30Lcam cannot be easily determined; however, it is important to note that the EP flux is not the same in these two simulations.

Aside to changes in the model's dynamics, changes in temperature in 60Lcam can result from changes in radiative heating in the model. The summer hemisphere warming near the tropopause is associated with changes in water vapor distribution in this region. Figures 9c and 9g show the difference in water vapor between 60Lcam and 30Lcam. In DJF and JJA, in the extratropical lower stratosphere in the summer hemisphere, water vapor decreases by 20–50% in 60Lcam as compared to 30Lcam. In the winter extratropical stratosphere, there is also a reduction in water vapor but only by 10–30%. A strong association between reduced water vapor and an increase in temperature was noted by Stenke et al. [2008]. In the Tropics, in DJF, there is a small increase in water vapor right above the tropopause, whereas in JJA, there is a 10% decrease.

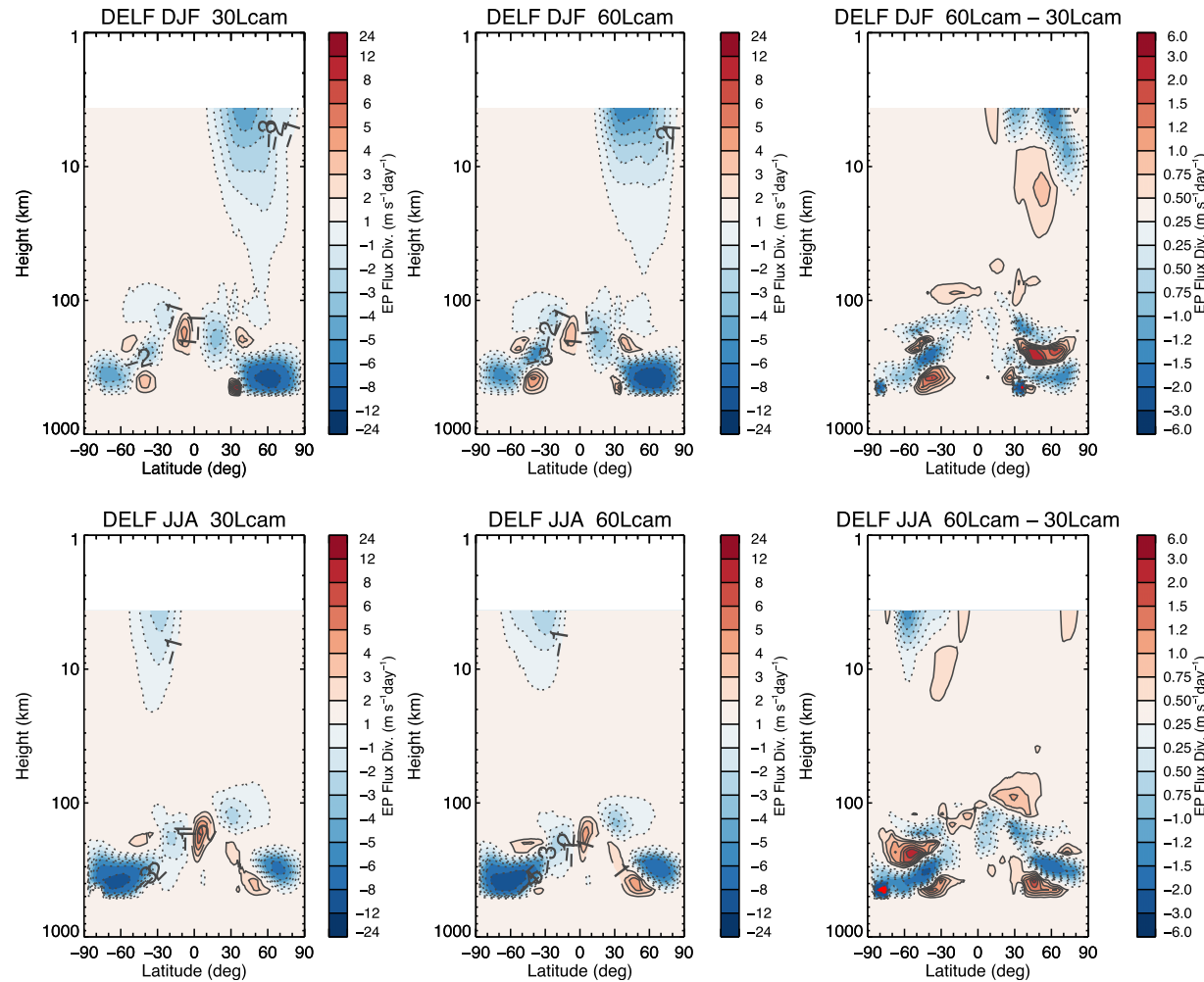


Figure 10. EP flux divergence $(\rho_0 \cos \phi)^{-1} \nabla \cdot \mathbf{F}$, for (top plots) DJF and (bottom plots) JJA for (left plots) 30Lcam, (center plots) 60Lcam, and (right plots) their difference. Units are $\text{m s}^{-1} \text{d}^{-1}$.

To get further insight into the cause of the differences between the 30 level and 60 level CAM, we examine the TEM zonal mean temperature equation, following Andrews *et al.* [1987]:

$$\bar{\theta}_t + a^{-1} \bar{v}^* \bar{\theta}_\phi + \bar{w}^* \bar{\theta}_z - \bar{Q} = -\rho_0^{-1} \left[\rho_0 (\bar{v}' \bar{\theta}'_\phi / a \bar{\theta}_z + \bar{w}' \bar{\theta}') \right]_z \quad (8)$$

where θ is the potential temperature, and \bar{Q} is the total heating rate. The term on the right-hand side (RHS) of equation (8) is a contribution to heating from non quasigeostrophic motions. This term is generally much smaller than the other terms in the equation. Hence, changes in temperature of the atmosphere result from two main tendencies: advective $(-(a^{-1} \bar{v}^* \bar{\theta}_\phi + \bar{w}^* \bar{\theta}_z))$ and radiative and diabatic heating (\bar{Q}). We have calculated these tendencies for the 30Lcam and 60Lcam from daily mean output for 20 years of these simulations. In CAM5, \bar{Q} consist of radiative heating, moist heating, dissipation heating from parameterized gravity waves, and diffusion. Short-wave and long-wave radiative heating are the primary components of \bar{Q} in the stratosphere. In the tropopause region, heating from moist processes becomes important. The other heating terms are negligible by comparison.

Figure 11 shows the balance of the terms in the TEM zonal mean temperature equation (equation (8)) averaged over four regions of the atmosphere defined as: Region 1: 80°S–88°S and 10–100 hPa, Region 2: 80°N–88°N and 10–100 hPa, Region 3: 30°S–88°S and 120–230 hPa, and Region 4: 30°N–88°N and 120–

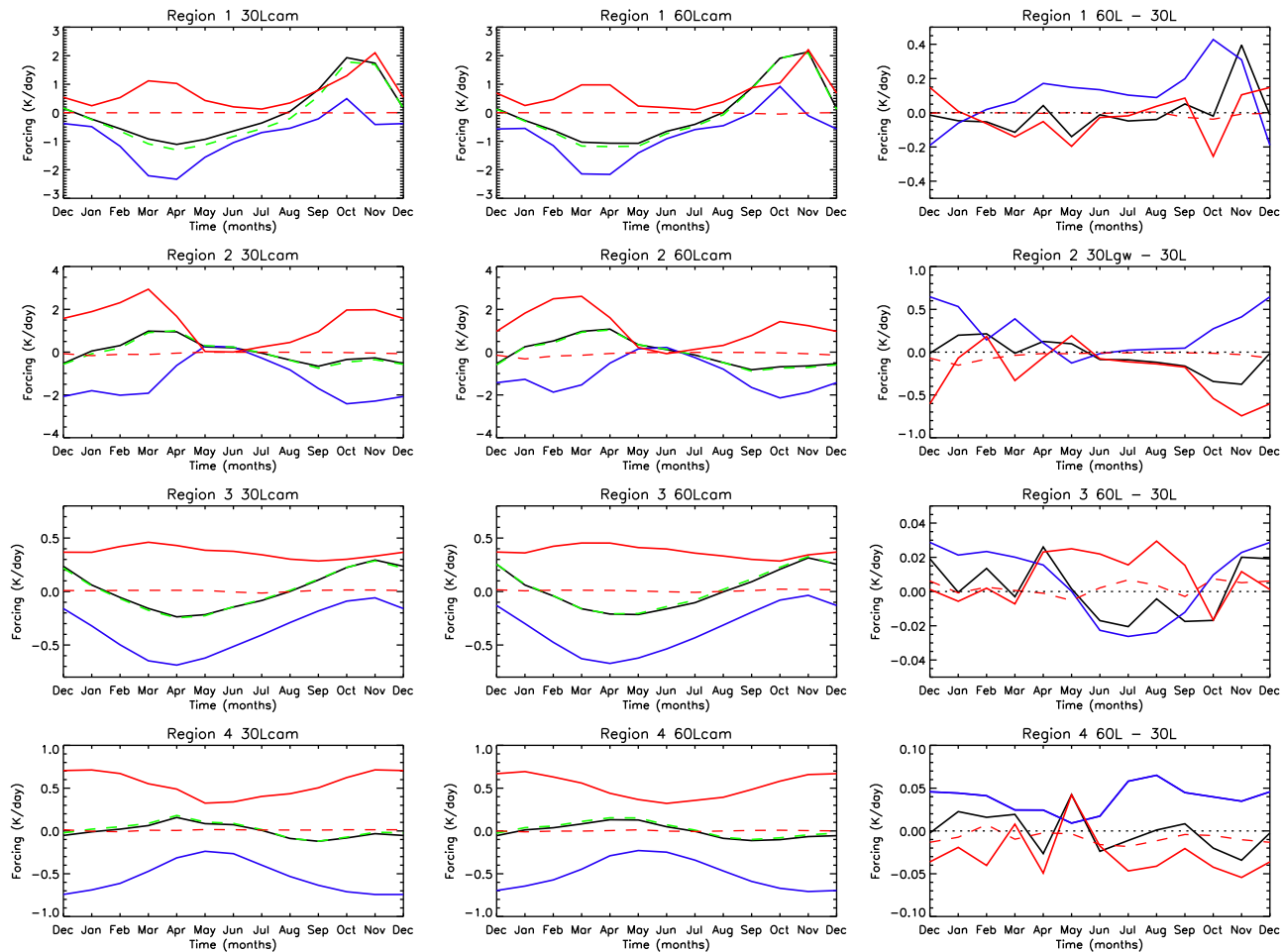


Figure 11. Balance of terms in the TEM zonal temperature equation equation (8). The thick black line is $\bar{\theta}_t$, the red thick line represents the total advective term, $-(\sigma^{-1}\bar{v}^*\bar{\theta}_\phi + \bar{w}^*\bar{\theta}_z)$, the thick blue line represents the total heating, \bar{Q} , and the dashed red line represents the RHS of (8). The green dashed line shows the total of thick red, thick blue, and dashed red line. The dotted black line is a zero line. The averaging regions as follows: Region 1: 80°S – 88°S and 10–100 hPa, Region 2: 80°N – 88°N and 10–100 hPa, Region 3: 30°S – 88°S and 120–230 hPa, and Region 4: 30°N – 88°N and 120–230 hPa.

230 hPa. It is clear from the left and center plots of Figure 11 that the advective term in the zonal mean temperature equation is always a positive term and is nearly balanced by the negative radiative tendency. Note that even though many of our temperature tendency terms are highly derived quantities, there is an excellent agreement between the calculated $\bar{\theta}_t$ (black line) and the total of tendencies derived from model output (dashed green line). The balance of advective and radiative terms is qualitatively very similar for the 60Lcam and 30Lcam (middle column of Figure 11); however, there are small differences in each one of the regions of interest. In Region 1, in the stratosphere near the South Pole, there is $\sim 10\%$ less radiative cooling in 60Lcam compared to 30Lcam in all months except for December and January. In Region 2, in the Northern Hemisphere's polar stratosphere, the changes are more substantial: advective and radiative tendencies in November, December, and January are 30% less in the 60Lcam as compared to 30Lcam. In Region 3, the tropopause region in the Southern Hemisphere, the tendency terms of the TEM zonal mean temperature equation differ by about 10%: the tendencies are bigger (smaller) during Southern Hemisphere's winter (summer). In Region 4, the changes in temperature tendency terms between the 60 level and 30 level CAM5 are the smallest, however consistent throughout the year: they are reduced by 5–10%. The changes in \bar{Q} shown in Figure 11 are related to the changes in the amount of water vapor and clouds in the atmosphere in Regions 3 and 4. The reduction of lower stratospheric water vapor in the extratropics, leads to decreased cooling (an increased \bar{Q}) in Region 4 throughout the year. This is also true in Region 3 in DJF, however not in JJA. As we will show in section 4.1, this likely is caused by changes in the long-wave cloud forcing in this region.

Overall, the increase in vertical resolution does not lead to qualitative differences in the annual cycles and balances of the heating tendencies shown in Figure 11. Nevertheless, small changes in the tendencies are associated with large seasonal mean temperature differences. The clearest connection between tendency changes and temperature changes with resolution exists in the northern winter stratosphere (Region 2). Here there is a clear reduction in advective warming, likely due to reduced descent. This is accompanied by reduced cooling and lower temperatures. The same dynamic but with opposite sense is clear in Region 3 (SH tropopause) during JJA, where increased advective warming is accompanied by increased cooling/higher temperatures. It is tempting to conclude that in these regions increased vertical resolution has altered the meridional circulation which then leads to corresponding temperature and radiative forcing changes. However, in the summer tropopause regions a different dynamic seems to be at work. Here we see increased temperatures in 60Lcam accompanied by stronger diabatic heating. This suggests that in this region, diabatic heating changes may be driving the temperature changes, rather than responding to them.

In summary, the above analysis shows that increasing the model's vertical resolution has a profound impact on the mean wind and temperature structure, especially in the extratropical upper troposphere and lower stratosphere, as well as in the winter polar stratosphere. With increased vertical resolution, the temperature budget of the atmosphere changes significantly: the largest differences occur in the Northern Hemisphere, above 100 hPa.

3.4. Combined Effects of Gravity Waves and Vertical Resolution

With simulation 60LcamGW, we examine the combined effects of gravity waves and increased vertical resolution on the mean climate in CAM5. Figures 2d and 2h show that the effects of gravity waves and of increased vertical resolution on the mean temperature structure of the atmosphere are more or less additive. The temperature differences in 60LcamGW relative to 30Lcam are very similar to those in 60Lcam except for the polar winter hemisphere, where nonorographic waves induced a strong warming. Figure 3d shows that in 60LcamGW, in DJF, the biases in temperature relative to ERA interim, between 100 and 10 hPa, are 2 K or less, and hence are much smaller than in our control simulation, 30Lcam. The cold tropopause bias in the Southern Hemisphere has improved by 2 K. In JJA, the simulation is also improved in the winter stratosphere, except of the now slight warm bias near 60°S, and the polar tropopause temperature biases are reduced by nearly 4 K.

Figures 5d and 5h show the zonal mean wind biases relative to ERA Interim for 60LcamGW. Compared to 30LcamGW there is an increased bias in tropical winds between 10 and 50 hPa in both DJF and JJA. This is associated with the changes in the variability of tropical winds which will be discussed in section 5.1. In the extratropics, in DJF there is a reduction in the too strong bias of winds upward of 300 hPa by about 2 m s^{-1} . In JJA, the improvements in the simulation are more obvious: the too strong bias in the northern hemispheric winds above 200 hPa is reduced by 2 m s^{-1} and the too strong winds between 30°S and 60°S and 200 and 50 hPa are improved. However, in 60LcamGW, there is a bigger bias in the zonal mean wind near the South Pole above 20 hPa.

3.5. Surface Stresses

Shaw and Shepherd [2007] and Shaw *et al.* [2009] have shown that changes due to nonorographic gravity wave breaking in a GCM can affect the surface through downward control and changes in downwelling. In our experiments, these effects are the largest during Southern Hemisphere winter. As was shown in section 3.2, in JJA there is a reduction of the upper tropospheric and lower stratospheric jet near 60°S. In JJA in 30LcamGW and 60LcamGW, this jet reduction reaches the surface with wind differences of 1 m s^{-1} relative to 30Lcam. These differences are large enough to cause significant changes to the surface wind stresses in this region. These are illustrated in Figure 12. Figure 12 shows that both, the presence of nonorographic gravity waves, and increased vertical resolution, tend to decrease the surface stresses in the Southern Hemisphere storm track region. The decrease in surface stress magnitude is fairly uniform with longitude in 30LcamGW (Figure 12b), whereas in 60Lcam the decrease is primarily in the central Southern Ocean and South Pacific Ocean (Figure 12c). In 60Lcam and in 60LcamGW, there is also a reduction of surface wind stresses in the western Arabian Sea. The reduction of the surface wind stresses in 30LcamGW, 60Lcam, and 60LcamGW significantly reduce CAM5's biases of this quantity relative to observations. Excessively strong surface stress has been a long-standing bias in CAM and it is coupled version (CCSM) as pointed out by Yeager *et al.* [2006]. Figure 13 shows JJA observations of the Large and Yeager [2009] (hereafter LY) surface

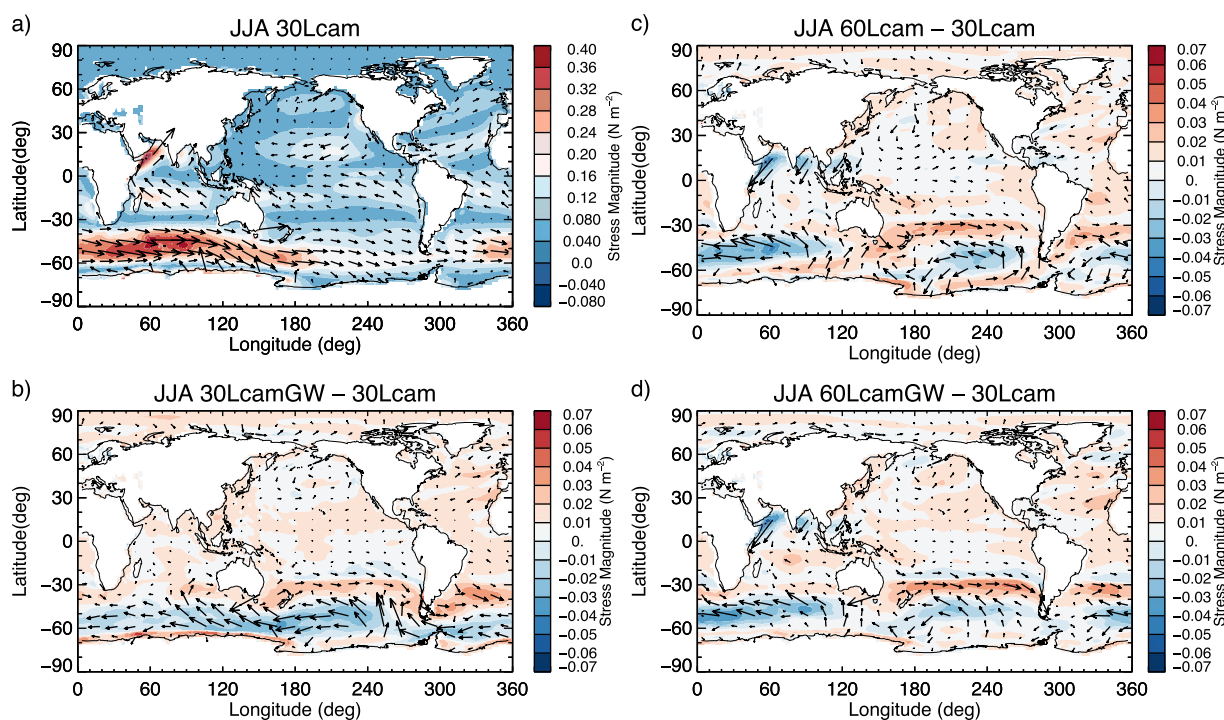


Figure 12. (a) Surface wind stress for JJA for 30Lcam and (b) surface wind stress differences from 30Lcam for 30LcamGW, (c) 60Lcam, and (d) 60LcamGW. The arrows depict the zonal and meridional components of the wind stress, whereas the wind stress magnitude is contoured.

stress observations and the departures from it for 30Lcam, 30LcamGW, and 60LcamGW. Our control simulation, 30Lcam, has a bias of 0.06 to 0.12 $N\ m^{-2}$ throughout the Southern Hemisphere's storm tracks. These biases are reduced to 0.02–0.08 in 30LcamGW and 60LcamGW.

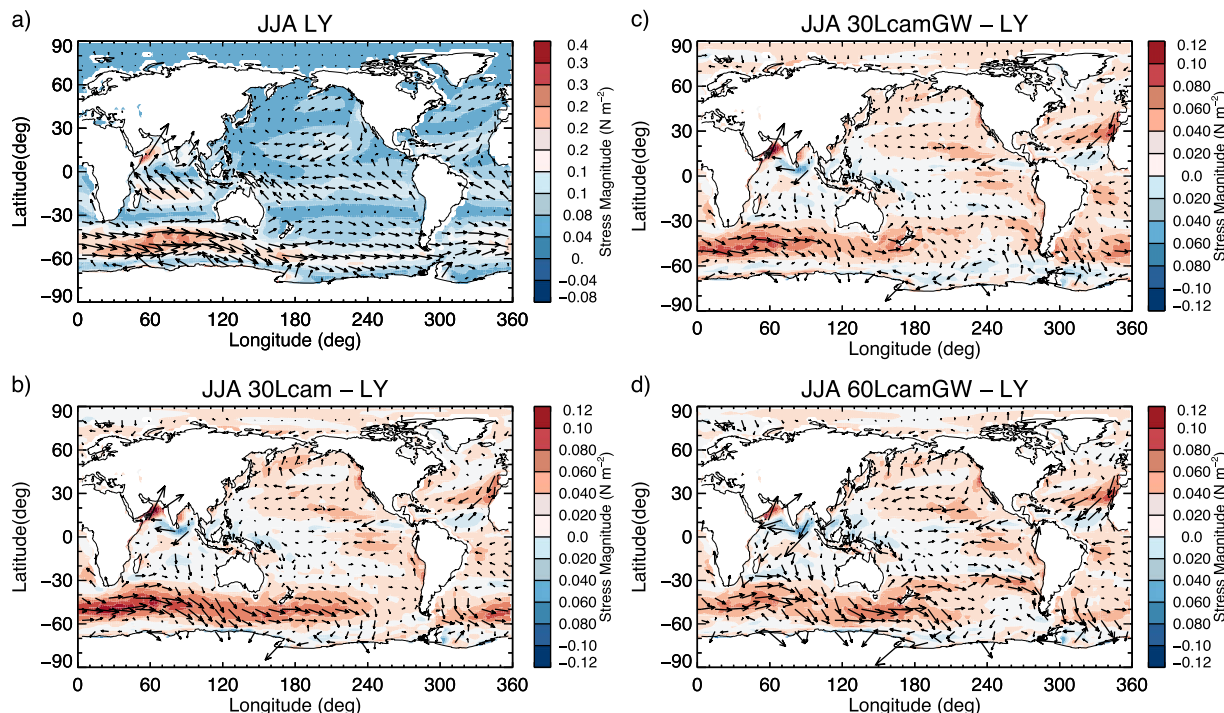


Figure 13. (a) Observed surface wind stress for JJA for 30Lcam and (b) surface wind stress differences from observations for 30LcamGW, (c) 60Lcam, and (d) 60LcamGW. The arrows depict the zonal and meridional components of the wind stress, whereas the wind stress magnitude is contoured. Observations consist of the Large and Yeager [2009] data set.

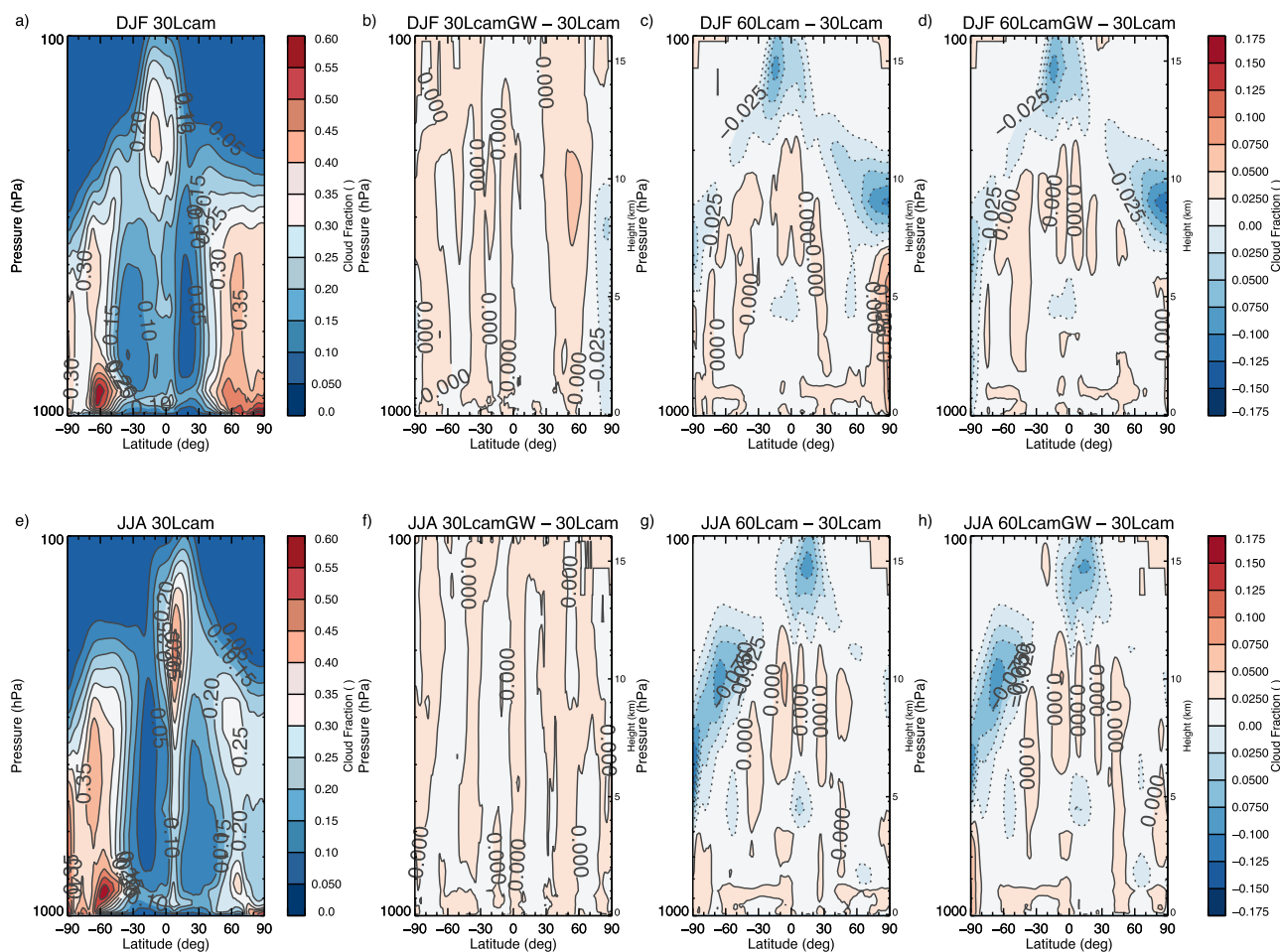


Figure 14. (a and e) Cloud fraction for 30Lcam and cloud fraction differences from 30Lcam for (left) 30LcamGW and (right) 60LcamGW. (top) DJF and (bottom) JJA.

4. Tropospheric Physics

Effects of nonorographic gravity waves and increased vertical resolutions have effects on the tropospheric climate beyond the mean wind and temperature structure. In this section, we highlight the most pronounced changes to the tropospheric climate in our experiments.

4.1. Clouds

Changes in distribution of clouds are tightly linked to those of temperature and humidity in our model. In 30LcamGW (Figure 2b), in DJF, there is a 2 K cooling at the tropopause near 60°N, and warming between 80°N and 90°N. This is associated with an increase in cloud fraction of 0.05 near 60°N and reduction of cloud fraction between 80°N and 90°N (Figure 14b). In JJA, there are virtually no changes in cloud fraction (Figure 14f) corresponding to the lack of changes in the tropospheric temperatures (Figure 2f).

Figures 14c, 14d, 14g, and 14h show that the cloud fraction decreases by up to 0.125 (30–50%) along the tropopause in the 60Lcam and 60LcamGW. The largest changes are near the winter polar tropopause both in DJF and JJA. The changes in cloud fraction relative to 30Lcam occur right below the regions of near-tropopause temperature increase noted in Figure 2. The temperature changes are largest in the extratropics (3–4 K) and smaller above the tropical Tropopause (1–2 K). In the free troposphere, there is cooling in the Tropics, but it is very weak, 1 K or less. In this region, relative humidity does not change (not shown), hence there are no differences in cloud fraction between the 30 level and 60 level models. It is clear from Figure 14 that the majority of changes in the cloud fraction in 60LcamGW come from the increased vertical resolution and have little to do with the addition of nonorographic gravity waves.

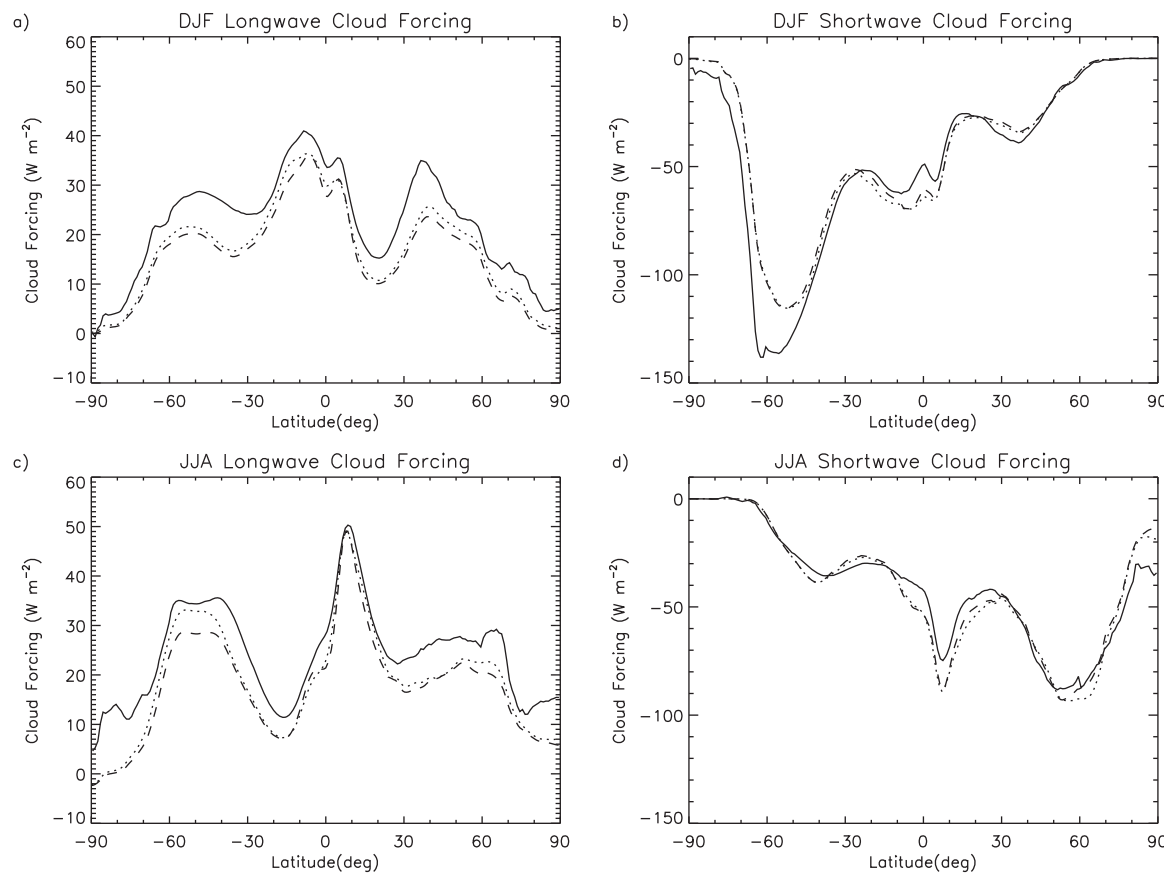


Figure 15. (left) Long-wave and (right) short-wave cloud forcing for CERES-EBAF (solid line), 30Lcam (dotted line), and for 60LcamGW (dashed line). (top) DJF and (bottom) JJA. Units are W m^{-2} .

Figure 15 shows the long-wave and short-wave cloud forcing (hereafter LWCF and SWCF, respectively) for 30Lcam and 60LcamGW and compares it to the CERES-EBAF data set [Loeb *et al.*, 2009]. The left plots of Figure 15 show that LWCF in CAM is around 5 W m^{-2} lower than CERES-EBAF observations more or less uniformly with latitude. Tropical LWCF during JJA is somewhat better simulated. The LWCF bias is intensified by around 1 W m^{-2} in 60LcamGW at most latitudes. LWCF in the southern storm track during JJA (40°S – 55°S , Figure 15c) is somewhat more sensitive to resolution with a 5 W m^{-2} decrease evident in 60LcamGW compared to 30Lcam. The short-wave cloud forcing in CAM5 is generally in good agreement with observations, except for the Southern Hemisphere's storm track region in DJF, where CAM5 underestimates the SW cloud forcing. The changes in 60LcamGW relative to 30Lcam are very small.

The sensitivity of LWCF and SWCF to vertical resolution is roughly consistent with the cloud fraction changes in Figure 14. The decreases in LWCF in 60LcamGW result from reductions in middle and high cloud, which are especially pronounced in winter high latitudes and in particular during JJA. Outside of wintertime, high-latitudes cloud fraction reductions with vertical resolution are small, except in the tropics near 100 hPa. We expect that these modest reductions in cloud fraction affect only thin clouds, which have very little impact on radiative forcing. It is also important to note that the microphysics in CAM5 has been tuned to produce reasonable representation of clouds in the 30 level model. This is likely the reason that the improvements in the representation of upper tropospheric temperatures in the 60 level CAM5 did not translate to improvements in cloud forcing.

4.2. Precipitation

Changes in upper tropospheric temperatures and clouds are associated with changes in the surface precipitation. As with tropospheric temperature changes, precipitation changes in the 30LcamGW simulation are

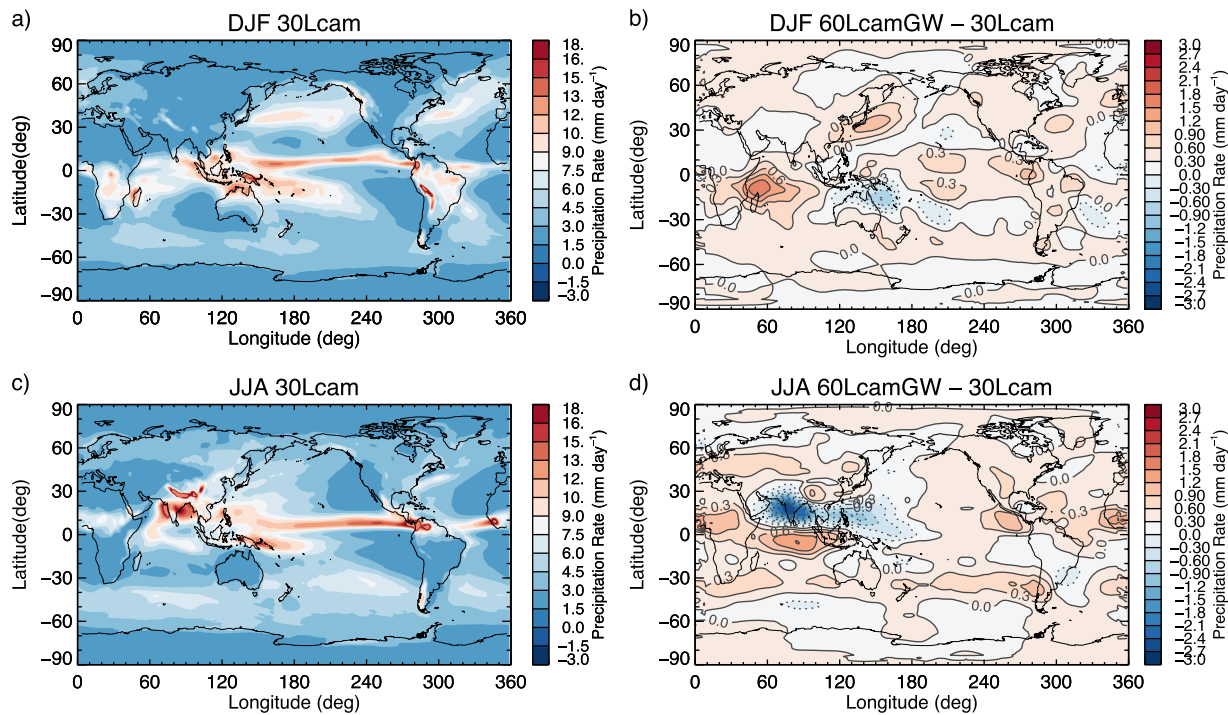


Figure 16. (left) Precipitation rate in mm d^{-1} for 30Lcam and (right) precipitation rate differences from 30Lcam for 60LcamGW. (top) DJF and (bottom) JJA.

minor. However, we see some impact on precipitation from increased vertical resolution. Figure 16 shows the DJF and JJA precipitation rate for 30Lcam and the changes relative to this simulation in 60LcamGW. Figure 17 shows the biases from the GPCP data set [Huffman *et al.*, 1997; Xie *et al.*, 2003] for these two simulations.

Significant impacts are present in the Indian Ocean and tropical western Pacific. The impact of increased vertical resolution is mixed. Positive biases in the western Indian Ocean during JJA are somewhat reduced, while negative biases in the western Pacific are exacerbated (Figures 17b and 17d). Unfortunately during DJF, widespread positive tropical precipitation biases in CAM appear to be generally worse in 60LcamGW than in 30Lcam, particularly immediately east of Africa where precipitation increases by around 1.5 mm d^{-1} .

Generally speaking, the largest impacts on precipitation from vertical resolution occur in the Indian monsoon region and western Pacific. This decrease in precipitation is likely due to decreased winds in this region and hence decreased moisture convergence.

5. Variability

5.1. Tropical Winds

In sections 3.3 and 3.4, we have noted significant changes in the tropical zonal mean winds in the 60Lcam and 60LcamGW relative to 30Lcam. We explore these further by looking at the 20 year time series of zonal mean winds averaged between 2°S and 2°N above 100 hPa for all the CAM5 simulations. The changes in this region are so significant that we have devoted an entire separate publication to these findings [Richter *et al.*, 2014], so we only provide a short summary of our results here. From long-standing observations, we expect to see a Quasi-Biennial Oscillation (QBO) of the zonal winds in the tropical lower stratosphere. The observed QBO has an average period of 28 months, with typical maximum easterlies of -30 to -35 m s^{-1} and typical maximum westerlies of 15 – 20 m s^{-1} [e.g., Baldwin *et al.*, 2001]. Figure 18a shows that in 30Lcam, we only have weak persistent easterlies at the equator, similar to previous versions of NCAR's GCM.

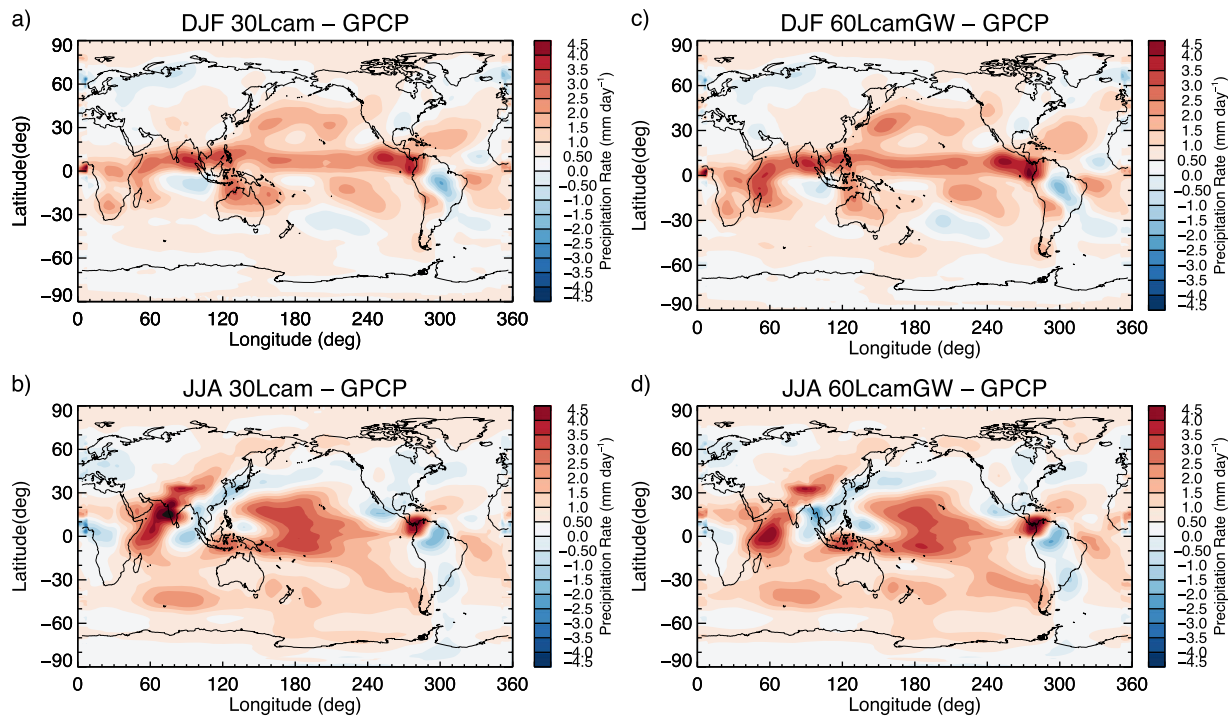


Figure 17. Precipitation rate difference from GPCP in mm d^{-1} for (left) 30Lcam and (right) 60LcamGW. (top) DJF and (bottom) JJA.

The addition of nonorographic gravity wave drag changes the tropical winds, especially near the model top (Figure 18b). Near the model top, above 10 hPa, where positive GW drag dominates, we now see primarily westerlies with magnitude of $3\text{--}8 \text{ m s}^{-1}$, and between 40 and 10 hPa, the winds oscillate between weak easterlies and weak westerlies. This oscillation does not resemble the QBO. In 60Lcam, however, the tropical winds near the model top become more easterly, and between 30 and 70 hPa, the simulation develops a layer of weak westerlies ($2\text{--}7 \text{ m s}^{-1}$). This is due to an increased upward propagation of, and momentum deposition from, Kelvin waves [Richter et al., 2014]. In 60LcamGW (Figure 18d), a clear QBO develops, with a period closely matching that of observations. The amplitude of the westerly phase of the QBO in 60LcamGW is stronger than observed by about 10 m s^{-1} , whereas the amplitude of the easterly phase is weaker than observed by about 10 m s^{-1} . As we show in detail in Richter et al. [2014], the QBO in 60LcamGW is driven by tropical mixed-Rossby gravity waves and Kelvin waves, as well as parameterized gravity waves. Both mixed-Rossby gravity waves and Kelvin waves can have vertical wavelengths as short as 2 or 3 km, and hence vertical resolution of at least 500 m in the free troposphere and lower stratosphere is needed to properly represent them. Clearly, the increase in vertical resolution in CAM5 to 500 m above 850 hPa in conjunction with the addition of nonorographic GW drag allows the model to better represent the tropical lower stratosphere.

5.2. Extratropical Zonal Wind and Temperature

The extratropical lower stratosphere exhibits a large seasonal cycle in both winds and temperature. Since the temperature gradient in the stratosphere is monotonic from pole to pole, the winds are westerly in the winter when temperatures are at their minimum and easterly in the summer. In the Northern Hemisphere, the winter circulation also has significant variability from December through March, due to the episodic occurrence of sudden stratospheric warmings (SSWs), characterized by a reversal of the zonal winds and rapid warming of a deep layer of the stratosphere [Charlton et al., 2007b]. In the top left plot of Figure 19, the seasonal cycle of zonal winds at 60N and 50 hPa, from ERA-Interim reanalysis [Dee et al., 2011] for the 20 year period 1980–1999 is compared with the corresponding time period from the 30Lcam and 60LcamGW simulations. The zonal winds at this location in 30Lcam are high relative to the reanalysis

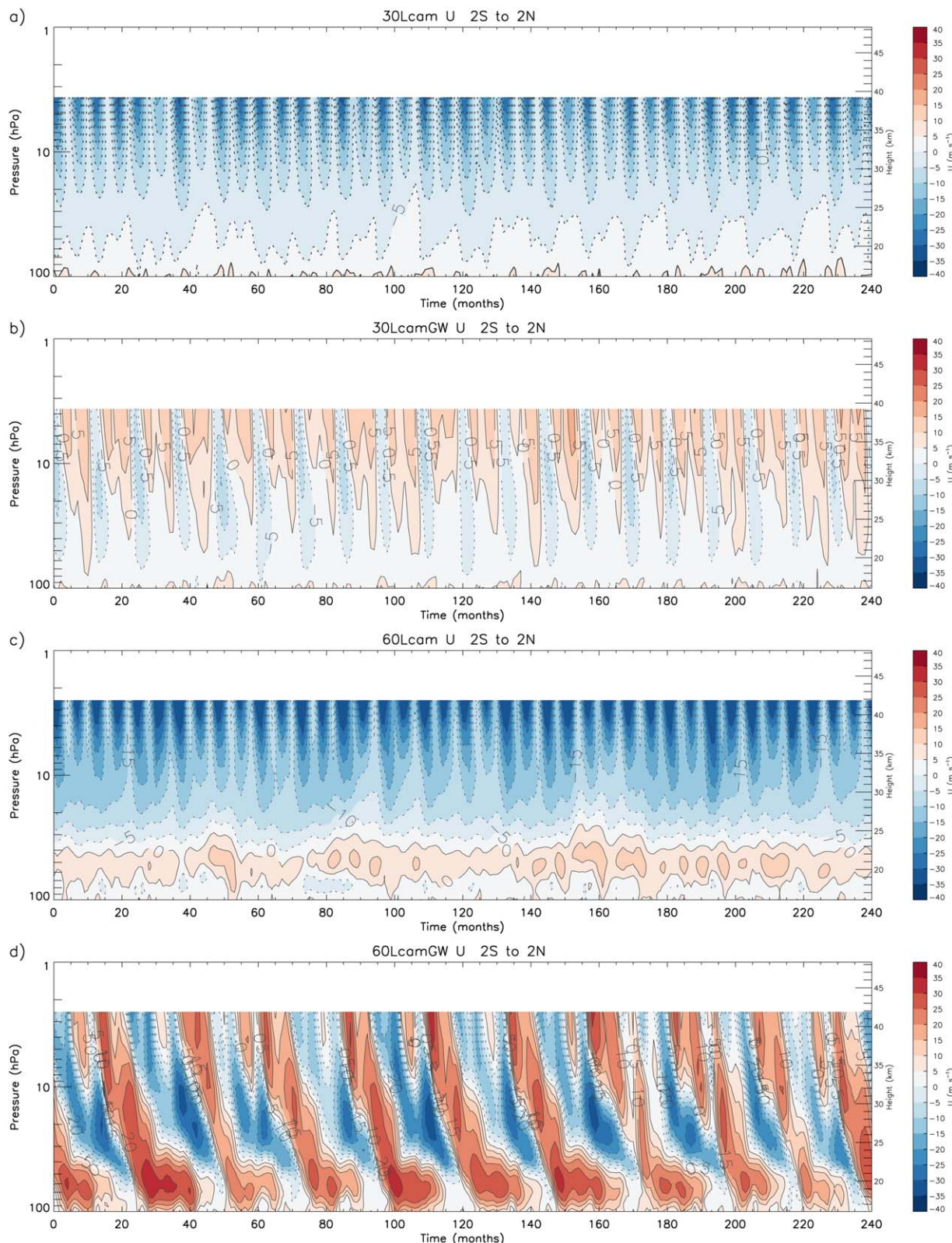


Figure 18. Tropical winds (2°S to 2°N avg) simulated by (a) 30Lcam, (b) 30LcamGW, (c) 60Lcam, and (d) 60LcamGW. The horizontal axis depicts time in months from 1 January 1979. Contours are plotted in intervals of 5 m s^{-1} .

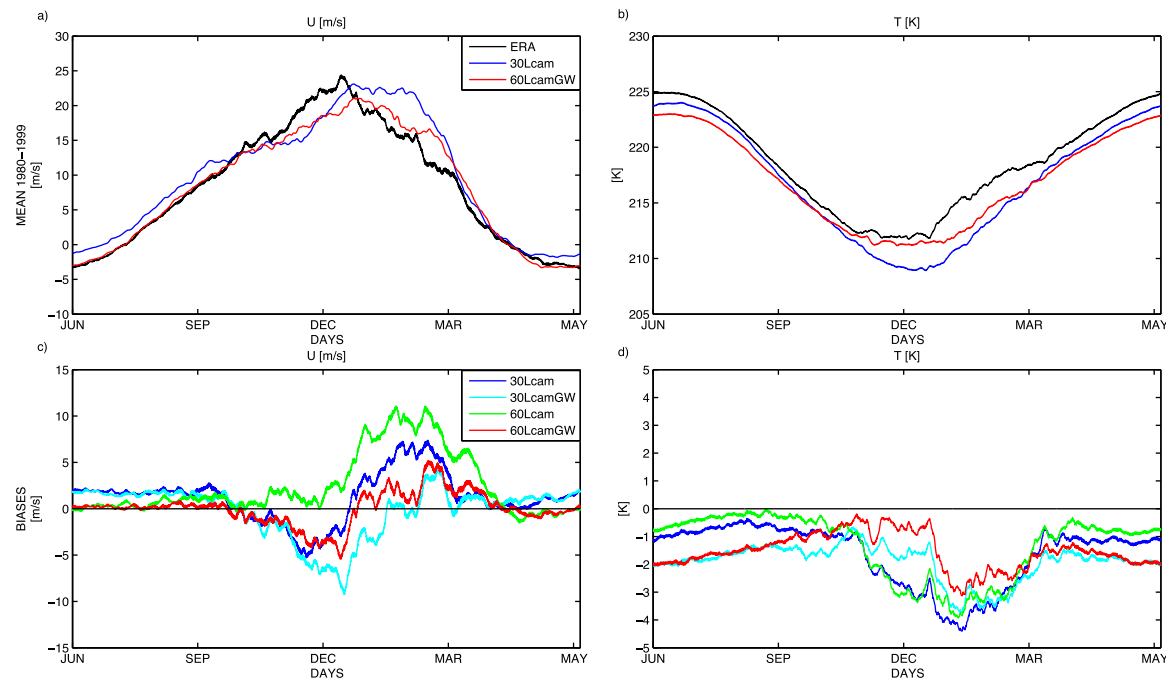


Figure 19. The seasonal cycle of (left) zonal mean wind and (right) temperature at 60°N latitude and 50 hPa altitude. (top) 20 year mean (1980–1999), 4 times daily values from ERA-Interim reanalysis (black), 30Lcam (blue), and 60LcamGW (red). (bottom) Bias relative to ERA-Interim reanalysis for 30Lcam (blue), 30LcamGW (cyan), 60Lcam (green), and 60LcamGW (red).

throughout much of the year, but too weak during the early portion of the winter. 60LcamGW matches the reanalysis much better throughout most of the year, although the bias toward weak winds in November and December is still evident. This early winter bias is due to the distribution of modeled SSWs, which will be discussed in greater detail in the next section.

The seasonal cycle of lower stratospheric, extratropical winds are strongly influenced by vertical resolution as well as the nonorographic gravity wave parameterization. This can be seen in the bottom left plot of Figure 19, where the bias from reanalysis is plotted for each of the four experiments. The 30LcamGW simulation shows a very similar bias to 30Lcam throughout much of the year, but the winds are weaker during the winter months. 60Lcam has very little bias during the summer; however, the winds are too strong during the winter. The right plots of Figure 19 show the corresponding comparison of the mean temperatures at 60°N and 50 hPa. Here we see that 30Lcam is too cold throughout the year, with a maximum bias in February of more than 4 K. 60LcamGW somewhat ameliorates the bias during midwinter; however, the summer stratosphere is even colder. This enhanced cold bias during the summer can be attributed to the parameterized gravity waves, since the 30LcamGW simulation (cyan) corresponds well with 60LcamGW, whereas 60Lcam is warmer than 30Lcam during the summer.

In the Southern Hemisphere, the seasonal cycle of temperature is important for modeling the ozone hole, since ozone chemistry is very sensitive to temperature. 30Lcam is too cold throughout the year, with a bias of more than 4 K during midwinter (Figure 20). 60LcamGW eliminates this midwinter bias, exhibiting excellent agreement with ERA-Interim from June through November. The zonal winds in 60LcamGW exhibit a slightly larger, positive bias than 30Lcam from June through September, which can be attributed to the effects of increased vertical resolution since they correspond so closely with the winds in the 60Lcam simulation (Figure 20).

5.3. Sudden Stratospheric Warmings

Planetary scale, atmospheric waves are evident in the polar stratosphere in both hemispheres during the winter months, and suppressed during the summer months when the winds aloft are easterly, inhibiting their vertical propagation [Charney and Drazin, 1961]. In the Northern Hemisphere, the resulting wave-mean flow interaction results in episodic wave breaking events or SSWs. First observed by Scherhag [1952], SSWs remain a challenge for the predictability of the Northern Hemisphere winter climate [Charlton et al., 2007b].

Table 1. Values of Several Metrics Adapted From Charlton *et al.* [2007a] Are Tabulated for ERA-Interim, 30Lcam, and 60LcamGW^a

DJF SSWs	ERA-I (1979–2011)	ERA-I (1979–1999)	30Lcam (1952–1999)	30Lcam (1979–1999)	60LcamGW (1952–1999)	60LcamGW (1979–1999)
Frequency (SSW/10 years)	6.1	5.5	2.7	4.0	2.5	2.5
ΔU_{10}	32.9	32.9	23.1	26.8	28.8	33.7
ΔT_{10}	8.1	9.2	4.2	3.5	5.1	3.2
ΔT_{100}	0.7	0.4	1.2	1.2	1.1	0.9
ΔNAM_{925}	-2.1	-2.3	-1.5	-1.5	-1.9	-1.6

^aValues are calculated for the entire data set/simulation as well as for the overlapping time period from 1979 to 1999. From top row to bottom: the frequency of DJF SSWs per 10 years, the change in zonal mean 10 hPa winds from 15 to 5 days prior to event minus the 5 days following the event (ΔU_{10}), the mean temperature anomalies at 10 and 100 mb during the 5 days centered on the event (ΔT_{10} and ΔT_{100}), and the minimum NAM value at 925 hPa during the 30 days following the SSW (ΔNAM_{925}).

Several metrics for comparing simulated SSWs are presented in Charlton *et al.* [2007b], including the change of the 10 hPa winds and temperatures during the course of the event. Another important metric is the distribution of SSWs throughout the winter season. Figure 21 shows the frequency of SSWs as a function of month for ERA-Interim (black), 30Lcam (blue), and 60LcamGW (red). Both these models have too many SSWs in November and March when compared with the reanalysis. The early winter SSWs in both of these models are reflected in the weaker than observed winds in the lower stratosphere during November and December, discussed in the previous section. The 30Lcam model also has no SSWs in February, which is the month when they are most frequently observed. This contributes to the bias toward too strong mean winds during midwinter in 30Lcam. These early and late season events also tend to evolve differently from the midwinter events that dominate the observed climatology. For this reason, we will restrict our subsequent discussion to events occurring in December, January, and February (DJF).

Table 1 lists a number of the metrics suggested by Charlton *et al.* [2007a] for comparing models with observations. We show statistics both from the entire length of ERA-I data set and model simulations, as well as for the overlapping time period from 1979 to 1999. We see that although both models exhibit $\simeq 5$ SSW/10 years when all events are identified according to the method of Charlton *et al.* [2007a], only half of those events occur during the midwinter. The changes in zonal winds and temperatures at 10 hPa (ΔU_{10}) are

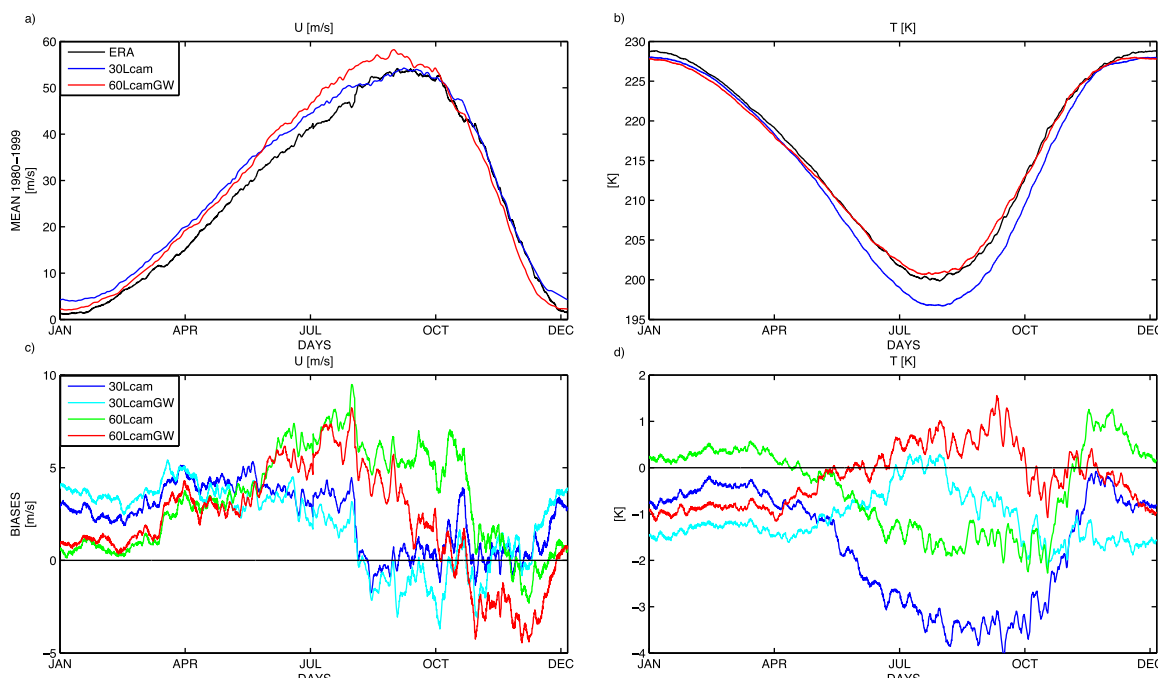


Figure 20. Same as Figure 19 with values at 60°S latitude and 50 hPa.

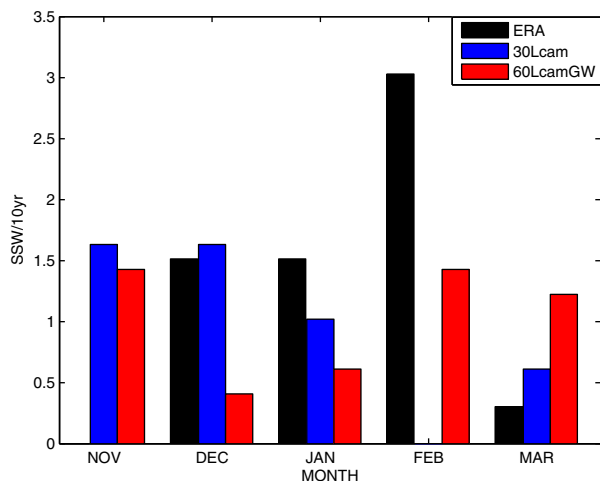


Figure 21. The frequency of sudden stratospheric warming events as a function of month for the ERA-Interim reanalysis (black), 30Lcam (blue), and 60LcamGW (red). Frequencies are reported in units of events per decade. Note that ERA-Interim spans years 1979–2011 whereas the model data set spans years 1952–1999.

high latitudes of the Northern Hemisphere. The NAM is defined here at each pressure level in the atmosphere, as the difference between mean geopotential height per unit area north of 65°N and south of 65°N . The climatological seasonal cycle has been removed and the index is normalized to have unit length. This definition is similar to that of Marshall [2003] for the Southern Hemisphere Annular Mode but can be defined at each pressure level. The near surface NAM responses for 30Lcam and 60LcamGW (ΔNAM_{925}) shown in Table 1, which have implications for the impact of SSWs on the tropospheric weather and climate following an event, are smaller (less negative) as compared to observations. The values in 60LcamGW are slightly closer to observations when considering the extended time period of analysis from 1952 to 1999. The NAM responses are actually more dissimilar between 30Lcam and the reanalysis in the free atmosphere than near the surface, as we will see in Figure 22.

The left column of Figure 22 shows the evolution of the zonal-mean zonal wind at 60°N as a function of height for the 30 days prior to and following the reversal of the westerly winds at 10 hPa. In the top row, the 20 observed DJF events from ERA-Interim are composited, the middle row is constructed from 13 midwinter events in 30Lcam and the bottom row reflects the 12 DJF events in the 60LcamGW simulation. The reanalysis shows a strong polar jet with wind speeds in excess of 40 m s^{-1} rapidly giving way to easterly winds that persist for several weeks. Both models show a reasonable evolution of the zonal winds, although the events do not last as long on average in the model as in the reanalysis. Temperature anomalies, composited in the second column of Figure 22 are calculated as the departure from the daily climatology. ERA-Interim suggests that midwinter SSWs typically follow colder than average temperatures at 60°N and positive temperature anomalies in excess of 5 K last for a week in stratosphere following the event. The temperature anomalies produced in the modeled SSWs are smaller in magnitude and evidence of a cold vortex prior to the event is not as apparent. SSWs have an influence on the winter climate of the Northern Hemisphere in the troposphere, as evidenced by a persistent negative annular mode anomaly in the troposphere following many events [Baldwin and Dunkerton, 2001]. This coupling between the stratosphere and troposphere is an ongoing subject of research and could provide some seasonal predictability if properly represented by models [Sigmund et al., 2013]. The right column of Figure 22 shows the familiar negative NAM response seen in reanalyses (top), as well as the simulated response from both models. Due to the small number of events, none of these anomalies are statistically significant, but the 30Lcam simulation shows very little NAM response while the 60LcamGW simulation at least has a negative sign throughout much of the troposphere during the 2 weeks following the composite event. Although neither model compares well to observations, the change in sign in the 60LcamGW model is encouraging evidence that the evolution of the wave breaking event and the consequent coupling with the troposphere are improving with enhanced vertical resolution.

comparable between 60LcamGW and ERA-I and they are somewhat lower in 30Lcam. Changes in temperature at 10hPa (ΔT_{10}) are about 50% lower in 30Lcam and 60LcamGW as compared to observations. The change in temperature at 100 hPa (ΔT_{100}) is a measure of the coupling between stratosphere and troposphere. This quantity is the only quantity that changes significantly between the different analysis periods for ERA-I (Table 1). Nevertheless, this value is overestimated in both 30Lcam and 60LcamGW. The above statistics suggest that there is little difference between SSWs in the 30 layer and the 60 layer CAM5.

The Northern Annular Mode (NAM) is the primary mode of variability in the

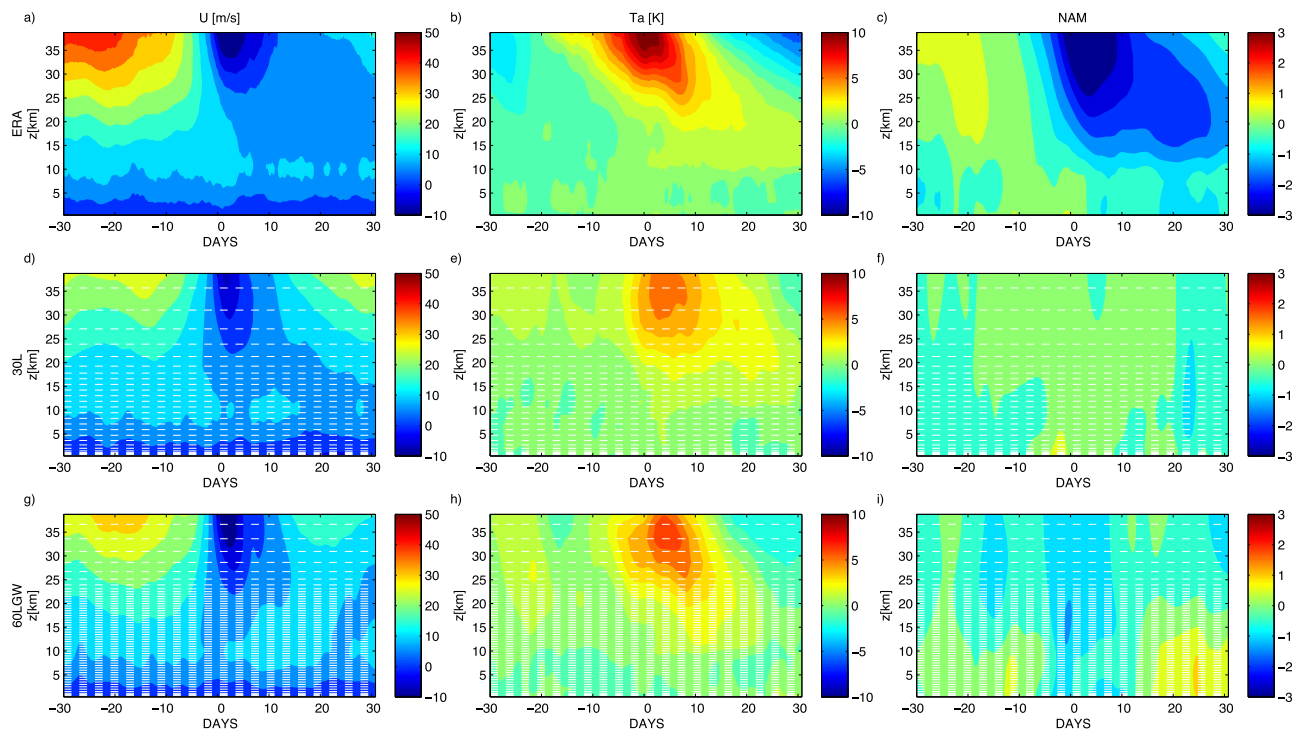


Figure 22. Composites of the (left) zonal mean wind, (center) temperature anomaly, and (right) annular mode during sudden stratospheric warming events identified in (top) ERA-Interim reanalysis, (middle) 30Lcam, and (bottom) 60LcamGW. The number of SSW events included in the analysis is 21 for ERA-Interim, 13 for 30Lcam, and 12 for 60LcamGW. Each figure shows the temporal evolution as a function of height, over a 60 day period centered on the date when the winds vanish at 10 mb. The white dotted lines in middle and bottom rows show the model levels.

6. Summary and Conclusions

We have examined here in detail the response of the climate simulation in CAM5 to changes in the model's vertical resolution and addition of nonorographic gravity wave drag. We find that both have a significant impact on the mean climate and variability of the upper troposphere and lower stratosphere, and the changes also affect surface wind stresses and precipitation. Increased vertical resolution in the free troposphere and lower stratosphere primarily causes warming in most of the model domain above ~ 200 hPa, except for the polar winter stratosphere, where cooling occurs. The warming near the tropopause region in the high vertical resolution model decreases CAM5's biases of tropopause temperatures by about 30%. Nonorographic gravity wave drag causes warming in the polar winter stratosphere of up to 8 K. The combination of nonorographic gravity waves and increased vertical resolution overall reduce CAM5's biases in mean temperature in the upper troposphere and lower stratosphere (Figure 3). The changes in temperature near the tropopause region are associated with changes in cloud fraction in CAM5. Cloud fraction is reduced near the polar winter tropopause both in DJF and JJA. Notable reduction in cloud fraction is also noted in the Tropics throughout the year. Increased vertical resolution in CAM5 also leads to changes in surface precipitation: in DJF, there is an increase in precipitation off the east coast of Africa, whereas in JJA, precipitation decreases over India, significantly improving CAM5's precipitation bias in this region.

Nonorographic gravity wave drag and increased vertical resolution also cause significant changes in mean wind in CAM5. Both changes, in JJA, decrease the Southern Hemisphere's midlatitude jet strength all the way to the surface which decreases the surface stresses near 60°S. This change is very important to the ocean-atmosphere coupling, as too strong surface stresses in the SH extratropics have been a long-standing bias in the NCAR GCM. The most significant change in the zonal mean wind in CAM5 occurs in the tropics: the combination of nonorographic gravity waves and increased vertical resolution allows the model to produce a QBO, a phenomenon that cannot be obtained in the 30 level CAM5 configuration or in the 60 level model without nonorographic gravity waves. The period of the QBO in 60LcamGW (CAM5 with

nonorographic gravity waves and high vertical resolution) matches observations closely; however, the westerly phase is too strong, and the easterly phase is a little too weak. A detailed analysis of the QBO in the 60 level model can be found in Richter et al. [2014].

Lastly, we examined the seasonal cycle of wind and temperature in the stratosphere at 60°S and 60°N as well as northern hemispheric sudden stratospheric warmings in CAM5. At 60°N, the best simulation of wind and temperature occurs in the CAM5 configuration with gravity waves and high vertical resolution, although the zonal winds in this simulation are still too weak in early winter, and slightly too strong in late winter. This improvement is primarily due to the nonorographic gravity waves. At 60°S, the cold temperature bias seen in 30L CAM5 disappears in 60LcamGW, however in this simulation, the zonal mean wind at 60°S and 50 hPa becomes too strong between April and September. These excessive winds appear to be related to the increased number of vertical levels, and not to the nonorographic gravity wave drag (Figure 20).

CAM5 has a relatively low model lid (near 2 hPa) and is hence not perfectly suited to examine SSWs; however, we still find it worthwhile to show that in the 60LcamGW the seasonal distribution of events is different in comparison with 30Lcam. In 30Lcam, the majority of SSWs occurs in November and December, and there are no warmings in February, during the month that there are most observed warmings. In 60LcamGW, there are also many warnings in November; however, there are also nearly 1.5 warnings per decade in February. In addition to changes in seasonal distribution, the NAM response during an SSW life-cycle is changed in 60LcamGW. Although this simulation still holds several biases from observations, it is a step in the right direction for improving stratospheric-tropospheric coupling in CAM5.

The simulations presented here were all performed with a stand-alone atmosphere model. The next step in our research will be to examine the effects of these model changes in a coupled atmosphere ocean model.

Acknowledgments

We thank Dave Williamson for providing a historical perspective on the vertical structure of NCAR's GCM. We thank the two anonymous reviewers for useful comments that helped to improve the manuscript. Partial support for this work was provided by Scientific Discovery through Advanced Computing (SciDac) program, funded by the U.S. Department of Energy, Office of Science, Advanced Scientific Computing Research.

References

- Andrews, D. G., J. R. Holton, and C. B. Leovy (1987), *Middle Atmosphere Dynamics*, Academic, San Deigo, Calif.
- Baldwin, M. P., and T. J. Dunkerton (2001), Stratospheric harbingers of anomalous weather regimes, *Science*, 294, 581–584.
- Baldwin, M. P., et al. (2001), The quasi-biennial oscillation, *Rev. Geophys.*, 39, 179–229.
- Beres, J. H., M. J. Alexander, and J. R. Holton (2004), A method of specifying the gravity wave spectrum above convection based on latent heating properties and background wind, *J. Atmos. Sci.*, 61, 324–337.
- Boville, B. A., and W. J. Randel (1992), Equatorial waves in a stratospheric GCM: Effects of vertical resolution, *J. Atmos. Sci.*, 49(9), 785–801.
- Bretherton, C., and S. Park (2009), A new moist turbulence parameterization in the Community Atmosphere Model, *J. Clim.*, 22(12), 3422–3448.
- Charlton, A. J., et al. (2007a), A new look at stratospheric sudden warming events. Part I: Climatology and modeling benchmarks, *J. Clim.*, 20, 449–469.
- Charlton, A. J., et al. (2007b), A new look at stratospheric sudden warming events. Part II: Evaluation of numerical model simulations, *J. Clim.*, 20, 470–488.
- Charlton-Perez, A. J., et al. (2013), On the lack of stratospheric dynamical variability in low-top versions of the CMIP5 models, *J. Geophys. Res.*, 20, 2494–2505.
- Charney, J. G., and P. G. Drazin (1961), Propagation of planetary-scale disturbances from the lower into the upper atmosphere, *J. Geophys. Res.*, 66, 83–109.
- Collins, W. D., et al. (2006), The formulation and atmospheric simulation of the Community Atmosphere Model: CAM3, *J. Clim.*, 19, 2144–2161.
- Collins, W. J., et al. (2011), Development and evaluation of an Earth-System model HadGEM2, *Geosci. Model Dev.*, 4, 1051–1075.
- Dee, D. P., et al. (2011), The ERA-Interim reanalysis: Configuration and performance of the data assimilation system, *Q. J. R. Meteorol. Soc.*, 165, 553–597.
- Dennis, J., J. Edwards, K. Evans, O. Guba, P. Lauritzen, A. Mirin, A. St-Cyr, M. Taylor, and P. Worley (2012), Cam-se: A scalable spectral element dynamical core for the community atmosphere model, *Int. J. High Performance Comput. Appl.*, 26(1), 74–89.
- Donner, L. J., et al. (2011), The dynamical core, physical parameterizations, and basic simulation characteristics of the atmospheric component AM3 of the GFDL Global Coupled Model CM3, *J. Clim.*, 24, 3484–3519.
- Easter, R. C., et al. (2004), Mirage: Model description and evaluation of aerosols and trace gases, *J. Geophys. Res.*, 109, D20210, doi:10.1029/2004JD004571.
- Fritts, D., and M. J. Alexander (2003), Gravity wave dynamics and effects in the middle atmosphere, *Rev. Geophys.*, 41(1), 1003, doi:10.1029/2001RG000106.
- Gettelman, A., et al. (2010), Global simulations of ice nucleation and ice supersaturation with an improved cloud scheme in the community atmosphere model, *J. Geophys. Res.*, 115, D18216, doi:10.1029/2009JD013797.
- Ghan, S. J., and R. C. Easter (2006), Impact of cloud-borne aerosol representation on aerosol direct and indirect effects, *Atmos. Chem. Phys.*, 6, 4163–4174.
- Giorgetta, M. A., E. Manzini, and E. Roeckner (2002), Forcing of the quasi-biennial oscillation from a broad spectrum of atmospheric waves, *Geophys. Res. Lett.*, 29(8), 1245, doi:10.1029/2002GL014756.
- Haynes, P. H., C. J. Marks, M. E. McIntyre, and T. G. Shepherd (1991), On the downward control of extra-tropical diabatic circulations by eddy-induced mean zonal forces, *J. Atmos. Sci.*, 48, 651–678.

- Hoskins, B. J. (1982), The mathematical theory of frontogenesis, *Annu. Rev. Fluid Mech.*, 14, 131–151.
- Huffman, G., et al. (1997), The Global Precipitation Climatology Project (GPCP) combined precipitation dataset, *Bull. Am. Meteorol. Soc.*, 78(1), 5–20.
- Iacono, M. J., J. S. Delamere, E. J. Mlawer, M. W. Shephard, S. A. Clough, and W. D. Collins (2008), Radiative forcing by long-lived greenhouse gases: Calculations with the AER radiative transfer models, *J. Geophys. Res.*, 113, D13103, doi:10.1029/2008JD009944.
- IPCC (2007), Climate change 2007: The physical science basis, in *Contribution of Working Group I to the Fourth Assessment Report of the Intergovernmental Panel on Climate Change*, edited by Solomon, S., D. Qin, M. Manning, Z. Chen, M. Marquis, K. Averyt, M. Tignor, and H. Miller, Cambridge Univ. Press, Cambridge, U. K. and New York.
- Large, W. G., and S. G. Yeager (2009), The global climatology of an interannually varying air-sea flux data set, *Clim. Dyn.*, 33, 341–364.
- Lindzen, R. S. (1981), Turbulence and stress owing to gravity wave and tidal breakdown, *J. Geophys. Res.*, 86, 9707–9714.
- Lindzen, R. S., and M. Fox-Rabinovitz (1989), Consistent vertical and horizontal resolution, *Mon. Weather Rev.*, 117, 2575–2583.
- Loeb, N., B. Wielicki, D. Doelling, G. Smith, D. Keyes, S. Kato, N. Manalo-Smith, and T. Wong (2009), Toward optimal closure of the earth's top-of-atmosphere radiation budget, *J. Clim.*, 22(3), 748–766.
- Marshall, G. J. (2003), Trends in the southern annular mode from observations and reanalyses, *J. Clim.*, 16(24), 4134–4143.
- McFarlane, N. A. (1987), The effect of orographically excited wave drag on the general circulation of the lower stratosphere and troposphere, *J. Atmos. Sci.*, 44, 1775–1800.
- Morrison, H., and A. Gettelman (2008), A new two-moment bulk stratiform cloud microphysics scheme in the Community Atmosphere Model, version 3 (CAM3). Part I: Description and numerical tests, *J. Clim.*, 21(15), 3642–3659.
- Neale, R. B., et al. (2012), Description of the NCAR Community Atmosphere Model (CAM 5.0), *Tech. Note NCAR/TN-486+STR*, Natl. Center For Atmos. Res., Boulder, Colo.
- Neale, R. B., et al. (2013), The mean climate of the Community Atmosphere Model (CAM4) in forced SST and fully coupled experiments, *J. Clim.*, 26, 5150–5168.
- Park, S., and C. S. Bretherton (2009), The university of Washington shallow convection and moist turbulence schemes and their impact on climate simulations with the community atmosphere model, *J. Clim.*, 22(12), 3449–3469.
- Pitcher, E. J., et al. (1983), January and July simulations with a spectral general circulation model, *J. Atmos. Sci.*, 40, 580–604.
- Pope, V. D., J. A. Pamment, D. R. Jackson, and A. Slingo (2001), The representation of water vapor and its dependence on vertical resolution in the Hadley Centre Climate Model, *J. Clim.*, 14, 3548–3554.
- Randel, W. J., and D. L. Williamson (1990), A comparison of the climate simulated by the NCAR Community Climate Model (CCM1:R15) with ECMWF analyses, *J. Clim.*, 3, 608–633.
- Richter, J. H., F. Sassi, and R. R. Garcia (2010), Towards a physically based gravity wave source parameterization in a general circulation model, *J. Atmos. Sci.*, 67, 136–156.
- Richter, J. H., J. T. Bacmeister, and A. Solomon (2014), On the simulation of the quasi-biennial oscillation in the Community Atmosphere Model, version 5, *J. Geophys. Res.*, 119, doi:10.1002/2013JD021122, in press.
- Rind, D., J. Lerner, J. Jonas, and C. McLinden (2007), The effects of resolution and model physics on tracer transports in the NASA Goddard Institute for Space Studies general circulation models, *J. Geophys. Res.*, 112, D09315, doi:10.1029/2006JD007476.
- Roeckner, E., et al. (2006), Sensitivity of simulated climate to horizontal and vertical resolution in the ECHAM5 atmosphere model, *J. Clim.*, 19, 3771–3791.
- Scherhag, R. (1952), Die explosionsartigen Stratosphärenerwärmungen des Spätwinters 1951/52, *Ber. Dtsch. Wetterdienstes US-Zone*, 6(38), 51–63.
- Schmidt, H. G., et al. (2006), The HAMMONIA Chemistry Climate Model: Sensitivity of the mesopause region to the 11-year solar cycle and CO₂ doubling, *J. Clim.*, 19, 3903–3930, doi:10.1175/JCLI3829.1.
- Shaw, T. A., and T. G. Shepherd (2007), Angular momentum conservation and gravity wave drag parameterization: Implications for climate models, *J. Atmos. Sci.*, 64, 190–203.
- Shaw, T. A., M. Sigmond, and T. G. Shepherd (2009), Sensitivity of simulated climate to conservation of momentum in gravity wave drag parameterization, *J. Clim.*, 22, 2726–2742.
- Sigmond, M., J. Scinocca, V. Kharin, and T. Shepherd (2013), Enhanced seasonal forecast skill following stratospheric sudden warmings, *Nat. Geosci.*, 6, 98–102.
- Stenke, A., V. Grewe, and M. Ponater (2008), Lagrangian transport of water vapor and cloud water in the ECHAM4 GCM and its impact on the cold bias, *Clim. Dyn.*, 31, 491–506.
- Taylor, M. A., and A. Fournier (2010), A compatible and conservative spectral element method on unstructured grids, *J. Comput. Phys.*, 229(17), 5879–5895.
- Williamson, D. L., and P. J. Rasch (1994), Water vapor transport in the NCAR CCM2, *Tellus, Ser. A*, 46, 34–51.
- Xie, P., J. Janowiak, P. Arkin, R. Adler, A. Gruber, R. Ferraro, G. Huffman, and S. Curtis (2003), GPCP pentad precipitation analyses: An experimental dataset based on gauge observations and satellite estimates, *J. Clim.*, 16(13), 2197–2214.
- Yeager, S. G., C. A. Shields, W. G. Large, and J. H. Hack (2006), The low-resolution CCSM3, *J. Clim.*, 19, 2545–2566.
- Zhang, G. J., and N. A. McFarlane (1995), Sensitivity of climate simulations to the parameterization of cumulus convection in the Canadian Climate Centre General Circulation Model, *Atmos. Ocean*, 3, 407–446.